THE ASTROPHYSICAL JOURNAL, 479:151–163, 1997 April 10

MORPHOLOGY AND DYNAMICS OF RELATIVISTIC JETS

J. M^{a}. MARTÍ[1] AND E. MÜLLER
Max-Planck-Institut für Astrophysik, Karl-Schwarzschild-Strasse 1, D-85748 Garching, Germany
J. A. FONT[2]
Departamento de Física Teórica, Universidad de Valencia, E-46100 Burjassot, Valencia, Spain
J. M^{a}. IBÁÑEZ
Departamento de Astronomía y Astrofísica, Universidad de Valencia, E-46100 Burjassot, Valencia, Spain
AND
A. MARQUINA
Departamento de Matemática Aplicada, Universidad de Valencia, E-46100 Burjassot, Valencia, Spain
Received 1995 October 16; accepted 1996 October 28

ABSTRACT

We present a comprehensive analysis of the morphology and dynamics of relativistic pressure-matched axisymmetric jets. The numerical simulations have been carried out with a high-resolution shock-capturing hydrocode based on an approximate relativistic Riemann solver derived from the spectral decomposition of the Jacobian matrices of relativistic hydrodynamics. We discuss the dependence of the jet morphology on several parameters, paying special attention to the relativistic effects caused by high Lorentz factors and large internal energies of the beam flow. The parameter space of our analysis is spanned by the ratio of the beam and ambient medium rest mass density (η), the beam Mach number (M_b), the beam Lorentz factor (W_b), and the adiabatic index (γ) of the equation of state (assuming an ideal gas). Both the ultrarelativistic regime ($W_b \geq 20$) and the hypersonic regime (relativistic Mach number greater than 100) have been studied.

Our results show that the enhancement of the effective inertial mass of the beam due to relativistic effects (through the specific enthalpy and the Lorentz factor) makes relativistic jets significantly more stable than Newtonian jets. We find that relativistic jets propagate very efficiently through the ambient medium, at speeds that agree very well with those obtained from an estimate based on a one-dimensional momentum balance. The propagation efficiency of a relativistic jet is an increasing function of the beam flow velocity.

Relativistic jets seem to give rise to two different morphologies, according to the relevance of relativistic effects. Hot beams (i.e., with internal energies comparable to the beam rest-mass energy) show little internal structure (as they are almost in pressure equilibrium with their surroundings) and relatively smooth cocoons forming lobes near the head of the jet. Highly supersonic models, in which the kinematic relativistic effects due to high beam flow Lorentz factors dominate, display extended cocoons that are overpressured with respect to the environment. The cocoon thickness decreases, and its mean pressure increases with increasing beam Lorentz factor.

Subject headings: galaxies: jets — hydrodynamics — methods: numerical — relativity

1. INTRODUCTION

The presence of continuous channels (jets) emanating from galactic nuclei and feeding the radio lobes in powerful double radio sources was postulated by several authors in the early seventies (e.g., Blandford & Rees 1974; Scheuer 1974). With the advent of the Cambridge 5 km telescope and the Very Large Array (VLA), kiloparsec-scale jets were discovered to be associated with more than 100 double radio sources (Bridle & Perley 1984). At this scale, the morphology of the observed jets varies from weak sources (i.e., Fanaroff-Riley class I sources; Fanaroff & Riley 1974) to powerful sources (Fanaroff-Riley class II radio galaxies and lobe-dominated radio-loud quasars). The most remarkable difference is that FR I sources tend to have prominent, smooth, continuous, two-sided jets running into the lobe structures, whereas powerful sources have usually one-sided (with a jet/counterjet flux density ratio greater than 4:1), knotty jets with bright outer hot spots (see, e.g., Muxlow & Garrington 1991). In core-dominated sources, where the luminous core is usually associated with a bright one-sided radio jet, very long baseline interferometric imaging has revealed a continuity between small- and large-scale structures, with inner parsec-scale one-sided jets proceeding to outer kiloparsec-scale jets. Features in these jets are observed to be moving away from the core at superluminal speeds in more than 40 sources (see, e.g., Ghisellini et al. 1993) to distances beyond 100 pc (as, e.g., in the quasar 3C 273; Davis, Unwin, & Muxlow 1991).

Within the nowadays accepted model (Blandford & Königl 1979), the superluminal motions and the jet asymmetries in compact sources are explained by assuming that one of the twin jets propagates with relativistic speed at a small angle to the line of sight toward the observer. In that case Doppler beaming of the emission in the direction of motion can account for the observed asymmetry in the luminosity of the jets. In addition, because of a purely kinematic relativistic effect, any feature moving with highly relativistic speed along the jet toward a distant observer appears to have a superluminal propagation velocity.

[1] Present address: Departamento de Astronomía y Astrofísica, Universidad de Valencia, E-46100 Burjassot, Valencia, Spain.
[2] Present address: Max-Planck-Institut für Gravitationsphysik, Schlaatzweg 1, D-14473 Potsdam, Germany.

Present observations of superluminal motion interpreted according to the beaming hypothesis lead to the conclusion that compact radio jets have bulk flows with Lorentz factors as large as 10.

Additional, independent indications of highly relativistic speeds can be derived from the intraday radio variability occurring in more than a quarter of all compact extragalactic radio sources (Krichbaum, Quirrenbach, & Witzel 1992). According to Begelman, Rees, & Sikora (1994), if the observed intraday radio variability is intrinsic and results from incoherent synchrotron radiation, the associated jets must have bulk Lorentz factors in the range ~ 30–100.

Whether the relativistic flows inferred from radio jets at parsec scales extend to kiloparsec distances is still an unsolved question. The common belief is, however, that the most powerful sources (i.e., FR II radio galaxies and quasars), in which jet asymmetries are important, exhibit at least mildly relativistic flows on large scales. In fact, bulk flow velocities on the order of $0.7c$ have been found for several sources ($1928+738$, Hummel et al. 1992; 3C 179, Akujor 1992; $1055+201$, $1830+285$, $2209+080$, Hooimeyer et al. 1992). In the case of FR I sources, direct measurements of the proper motion of knots in the M87 jet performed with the VLA (Biretta & Owen 1990; Biretta, Zhou, & Owen 1995) have proved the existence of apparent superluminal motions out to a distance of ~ 1 kpc. According to these authors, the measurements are compatible with a kinematic model for the jet in M87 consisting of an inner jet (from the nucleus to knot A, located at ≈ 1 kpc) containing a high Mach number flow with a Lorentz factor ≥ 3 and a slower outer jet (Lorentz factor ≤ 2) beyond knot A. Such a relativistic inner jet could be responsible for the one-sidedness of the jet base seen in many FR I sources (see Muxlow & Garrington 1991). Finally, a decelerating relativistic jet model (Laing 1996) applied to the archetypical FR I source 3C 31 leads to an almost constant beam deceleration from $0.8c$ at distances less than 2 kpc from the nucleus, to $0.1c$ at larger distances (≈ 7 kpc).

Although the collisional mean free path is very large in the jet plasma, a hydrodynamic description of the jet flow is justified because of the presence of microgauss magnetic fields, which provide the collisional coupling of the plasma. In extragalactic jets, the Larmor radii and Debye lengths of positrons (or protons) and electrons are several orders of magnitude smaller than the jet widths (Begelman, Blandford, & Rees 1984). For this reason, hydrodynamic simulations have become an important tool in our understanding of the morphology and dynamics of extragalactic jets since Norman et al. (1982) verified the jet model of Blandford & Rees (1974) in their pioneering investigation. Meanwhile, hydrodynamic simulations have provided us with an understanding of structures observed in many VLA images of radio jets, and magnetohydrodynamic simulations have shown the importance of toroidal magnetic fields for the confinement of jets (Clarke, Norman, & Burns 1989; Lind et al. 1989; Kössl, Müller, & Hillebrandt 1990). The confinement properties of overpressured cocoons in hypersonic jets (see Begelman & Cioffi 1989) have been numerically investigated by Loken et al. (1992). Three-dimensional simulations (Balsara & Norman 1992) have been used to test models for narrow-angle–tail sources, whose complex morphologies are the result of the interaction of a supersonic jet with a cross wind (Begelman, Rees, & Blandford 1979). Norman, Burns, & Sulkanen (1988) and Loken et al. (1995) studied the morphologies of radio sources with wide-angle tails by means of two-dimensional (planar) and three-dimensional jet simulations. According to their models, the expansion and subsequent disruption of jets in wide-angle–tail sources results from the sudden change in the ambient pressure (probably due to a shock) occurring in the outer halo (i.e., for distances in the range 10–50 kpc) of a galaxy. Three-dimensional simulations (Cox, Gull, & Scheuer 1991) were also required to explore whether multiple hot spots can be produced by sideways motions of the jet (Scheuer 1982).

In the case of relativistic jets, numerical difficulties arising in the integration of the relativistic hydrodynamic equations have traditionally restricted the research to the stationary regime (Wilson 1987; Daly & Marscher 1988; Dubal & Pantano 1993; Bowman 1994). Only very recently have the first time-dependent simulations of relativistic jets been performed (van Putten 1993; Martí, Müller, & Ibáñez 1994; Eulderink & Mellema 1994; Duncan & Hughes 1994; Martí et al. 1995). Eulderink & Mellema (1994) proved the collimation of relativistic spherical outflows by thickened disks, but they did not discuss the morphological properties of the emerging jets. The remaining work dealt with initially well-collimated beams, but the parameter space covered by these simulations was very small. Van Putten (1993) performed a relativistic jet simulation with beam Lorentz factor 3.25 in slab symmetry. However, the jet propagation was followed only for a distance of 6–7 initial beam radii. Hence he was only able to verify the formation of a Mach disk at the end of the relativistic beam. Martí et al. (1994) and Duncan & Hughes (1994) have performed longer simulations in planar and cylindrical symmetry, which were restricted to low beam Mach number models. Both groups derived similar conclusions concerning the morphology of these relativistic models (e.g., lack of beam internal structure, steady propagation; see below). Finally, the morphology and dynamics of an extremely relativistic (flow Lorentz factor 22) highly supersonic jet has only recently been considered by Martí et al. (1995).

This work represents the first attempt to study the morphology and dynamical properties of relativistic jets for a wide range of initial parameters, paying special attention to relativistic effects that result from bulk flow velocities in the beam close to the speed of light and from relativistic internal beam energies.

The paper is organized as follows: In § 2, we summarize, for comparison, the main results concerning the morphology and dynamics of classical jets. The relativistic simulations are presented in § 3, which forms the body of the paper and also contains some theoretical considerations concerning the morphology and propagation properties of relativistic jets. The equations of relativistic hydrodynamics (in conservation form) in cylindrical symmetry, a brief description of the numerical method used to integrate the dynamical equations, and a discussion of the parameter space covered by the simulations appear also in § 3. The main conclusions of our study are given in § 4. The algorithm used in the calculation of the numerical fluxes is described in Appendix A. Finally, Appendix B contains a set of one- and two-dimensional test problems that our hydrodynamic code has successfully passed.

2. MORPHOLOGY AND DYNAMICS OF CLASSICAL JETS

In a series of papers (e.g., Norman et al. 1982; Norman, Winkler, & Smarr 1983; Norman, Smarr, & Winkler 1985;

Norman, Winkler, & Smarr 1984), Norman and collaborators presented a comprehensive study of the morphology and dynamics of pressure-matched classical jets propagating into a homogeneous medium, which was based on an extensive set of two-dimensional hydrodynamic simulations. Initial jet models were constructed by varying two parameters: the beam Mach number, M_b, and the density ratio $\eta \equiv \rho_b/\rho_m$ of the incoming beam gas to the ambient medium. Note that the third parameter, which then (for a given adiabatic index) completely specifies the flow, was fixed by assuming a pressure-matched jet, i.e., $K \equiv p_b/p_m = 1$, where p_b and p_m are the pressure of the beam gas and of the ambient medium, respectively. The models were scaled setting $\rho_m = c_{s,m} = R_b = 1$, where $c_{s,m}$ is the sound speed in the ambient medium. With this choice of scaling, the density, the sound speed, and the Mach number of the beam flow are dimensionless. The study covered one decade in M_b (from 1.5 to 12) and three decades in η (from 0.01 to 10; see, e.g., Fig. 1 of Norman et al. 1983).

A detailed picture of the morphology of supersonic jets was derived from the study. Supersonic jets are mainly composed of a supersonic beam that ends in a Mach shock, a cocoon made of shocked beam gas, a *working surface* (Blandford & Rees 1974) that separates beam and shocked ambient gas, and a bow shock. The propagation speed of the working surface defines the velocity of the jet itself.[3] According to these studies, for sufficiently light ($\eta \leq 0.1$), high Mach number jets, the high pressure of the shocked gas drives a backflow toward the source, which gives rise to an extended cocoon. The prominence of the cocoon diminishes when going from diffuse to dense jets ($\eta \geq 1$; see below). Holding the beam density fixed and reducing the beam Mach number makes the extensive cocoons turn into lobes of matter localized near the head of the jet.

The propagation velocity of the jet through the external medium can be estimated by equating the momentum flux of the beam gas and the external medium in the frame of the working surface. For pressure-matched jets, the Newtonian jet velocity, V_j^{N}, is then given by

$$V_j^{\mathrm{N}} = \frac{\sqrt{\eta}}{1+\sqrt{\eta}}\, v_b \qquad (1)$$

(see, e.g., Norman et al. 1983), where v_b is the fluid velocity within the beam. According to this formula, diffuse jets (i.e., η being small) would propagate at a small fraction of the beam flow velocity and only very dense jets will have propagation speeds close to the beam velocity. Note that equation (1) has been obtained on the basis of a head-on momentum transfer between beam and ambient gas only, disregarding any multidimensional effects such as, e.g., the sideways expansion of the head of the jet. Hence the estimate has to be considered as an upper bound of the actual jet propagation velocity. In the large sample of models studied by Norman et al. (1983), dense jets are seen to propagate most efficiently, their speed, however, never exceeding 80% of the one-dimensional estimate, whereas low Mach number diffuse jets appear to be less efficient ($\approx$40% of the one-dimensional estimate). Moreover, highly supersonic, diffuse jets suffer from a secular deceleration due to internal shocks present in these models. Their nonsteady propagation leads to the growth of vortices at the working surface due to Rayleigh-Taylor instabilities. Only hypersonic ($M_b \geq 30$), dense enough ($\eta \geq 0.03$) models, as considered by Massaglia, Bodo, & Ferrari (1996), seem to have propagation efficiencies greater than 1.0.

The mass flux across the terminal shock (which, integrated over time, yields to a good approximation the mass within the cocoon) is proportional to the beam fluid velocity relative to the Mach shock. Taking into account that the Mach shock propagates almost at the advance speed of the jet, equation (1) allows one to determine the relative prominence of the cocoon in classical jet models. Diffuse jets propagating at a small fraction of the beam flow velocity create a pileup of shocked beam material, which feeds a thick cocoon. Dense jets, on the contrary, have a small mass flux into the cocoon, leading to morphologies in which the beams are the most prominent element ("naked beams"). These simple considerations are confirmed by the numerical simulations (Norman et al. 1982, 1983).

According to the simulations, the beams show internal structure (Norman et al. 1985, 1984; see also Bodo et al. 1994). In diffuse, high beam Mach number models, the perturbations arising in the cocoon by Kelvin-Helmholtz instabilities of the cocoon/ambient gas boundary, or by the flow within the cocoon itself, produce a chaotic distribution of internal shocks. Periodic internal shocks can be produced by a pressure mismatch between beam and cocoon in stationary underpressured jets (see, e.g., Wilson & Falle 1985 and references cited therein). The main cause for the internal beam structure of models with naked beams are nonlinear pinching modes (i.e., axisymmetric) of the Kelvin-Helmholtz instability. Among those, models with a sufficiently small beam Mach number ($M_b < 2\eta^{0.3}$; Cohn 1983) are dominated by the fundamental mode, which is disruptive, while for models with $M_b > 2\eta^{0.3}$, the dominant reflecting mode saturates at finite amplitude, leading to the formation of a nearly periodic structure of biconical internal shock waves.

3. MORPHOLOGY AND DYNAMICS OF RELATIVISTIC JETS

The most obvious difference between classical and relativistic dynamics is the presence of a maximum velocity, i.e., the speed of light in vacuum, c, in the latter case. This implies that relativistic flows can no longer be scaled in space and time separately, but instead both scales are related by the speed of light. Hence, beyond K, η, M_b, and γ, an additional, fifth parameter is required to completely specify a relativistic jet propagating into a homogeneous medium. We chose the beam flow velocity, v_b, measured in units of c, to be this fifth flow parameter.

Similar to the classical case, an estimate of the jet velocity can be obtained by equating the momentum flux of the beam and the ambient gas in the frame of the working surface (see eq. [1]). Because both large specific internal energies (compared to c^2) and relativistic velocities are encountered, the physical principle established above reads

$$\rho_b h_b W_b'^2 v_b'^2 = \rho_m h_m W_m'^2 v_m'^2 \qquad (2)$$

for a beam in pressure equilibrium with the ambient medium, h and W being respectively the specific enthalpy and the flow Lorentz factor (see below). The subscripts m and b stand for ambient and beam, respectively. The primes indicate that the corresponding velocities are measured in

[3] In this paper, the velocity of the jet refers always to the advance speed of the jet through the ambient medium and should not be confused with the actual velocity of the material in the beam, which we refer to as the beam flow velocity.

the reference frame of the working surface. The (relativistic) velocity of the jet in the rest frame of the ambient medium, $V_j^R = -v'_m$, can be introduced in equation (2) by taking into account that the following relation between primed and unprimed velocities holds:

$$W'_b v'_b = W_j W_b (v_b - V_j^R) . \tag{3}$$

Then one has

$$\rho_b h_b W_b^2 (v_b - V_j^R)^2 = \rho_m h_m (V_j^R)^2 , \tag{4}$$

which, after some rearrangement, yields

$$V_j^R = \frac{\sqrt{\eta_R^*}}{1 + \sqrt{\eta_R^*}} v_b , \tag{5}$$

where η_R^* is defined as

$$\eta_R^* = \eta_R W_b^2 \tag{6}$$

and η_R is given by

$$\eta_R = \frac{\rho_b h_b}{\rho_m h_m} . \tag{7}$$

Note that, for fluids with nonrelativistic internal energies, η_R tends toward η and, for those having both nonrelativistic internal energies and nonrelativistic velocities, η_R^* tends toward η.

The first interesting result is that equation (5) produces systematically larger propagation velocities than its classical counterpart for the same initial beam data (see § 3.6). Applying the same reasoning as in § 2, this implies a reduction of the relevance of cocoons in relativistic models. Moreover, in the classical case, only dense (i.e., $\eta \gg 1$) jet models have propagation speed estimates close to the beam flow velocity. In the relativistic case, on the contrary, the condition $V_j^R \approx v_b$ is fulfilled whenever $(\eta_R^*)^{1/2} \gg 1$, i.e., for ultrarelativistic beam models, extremely hot jets, or both. This result is easily understood, because in relativistic dynamics both the internal energy and the Lorentz factor contribute to the increase of the *inertial mass density*.

An estimate of the total mass within the cocoon is given by the time integral of the mass flux across the terminal Mach shock. For a cylindrical flow of cross section πR_b^2 and for a constant beam flow given by the initial conditions, η, v_b, this estimate is

$$m_{\rm cocoon} = \pi R_b^2 \rho_b v'_b W'_b T' , \tag{8}$$

where T' is the total time measured in the reference frame of the Mach shock. In terms of quantities measured in the rest frame of the ambient medium, the previous equation reads

$$m_{\rm cocoon} = \pi R_b^2 \rho_b W_b (v_b - V_{\rm M}) T , \tag{9}$$

where $V_{\rm M}$ is the velocity of the Mach shock measured in the rest frame of the ambient medium.

If a comparison is to be made between different models at some epoch, say, when the jet has propagated along a distance L, then for each model the appropriate evolutionary time to be considered is $T = L/V_j^R$. Under these conditions the total mass within the cocoon scales as

$$m_{\rm cocoon} \propto \eta W_b (v_b - V_{\rm M})/V_j^R . \tag{10}$$

Taking into account that $V_{\rm M} \approx V_j^R$ and substituting the propagation speed of the jet by the estimate of equation (5), an extremely simple expression for the cocoon mass in terms of initial beam parameters can be derived:

$$m_{\rm cocoon} \propto \eta/\sqrt{\eta_R} . \tag{11}$$

Consistent with this expression is the result that hotter jets ($\eta_R \gg \eta$) will have increasingly less prominent cocoons. Moreover, the independence of the cocoon mass from the beam flow velocity, taken together with the larger densities of the shocked beam gas for increasing beam Lorentz factors, explains the thinner cocoons of faster jets.

In the following, we present the morphological and dynamical characteristics of relativistic jets derived from our numerical simulations. As we shall see, our results are consistent with the theoretical considerations discussed above.

3.1. *Hydrodynamic Equations, Numerical Techniques, and Initial Setup*

We have solved the equations of special relativistic hydrodynamics (units are chosen such that the speed of light $c \equiv 1$) for the conserved relativistic densities of rest mass, D, momentum, $\boldsymbol{S}$, and energy, τ,

$$D = \rho W , \tag{12}$$

$$\boldsymbol{S} = \rho h W^2 \boldsymbol{v} , \tag{13}$$

$$\tau = \rho h W^2 - p - D . \tag{14}$$

In the above equations, ρ, p, and $\boldsymbol{v}$ are the proper rest-mass density, pressure, and coordinate flow velocity, respectively. The flow Lorentz factor, W, and the specific enthalpy, h, are given by

$$W = \frac{1}{\sqrt{1 - \boldsymbol{v} \cdot \boldsymbol{v}}} , \tag{15}$$

$$h = 1 + \epsilon + (p/\rho) , \tag{16}$$

where ϵ is the specific internal energy.

The flow is supposed to be axisymmetric, and hence we use two-dimensional cylindrical coordinates (r, z). Expressed in this coordinate system and neglecting viscosity and thermal conduction, the relativistic hydrodynamic equations are

$$\frac{\partial D}{\partial t} + \frac{1}{r}\frac{\partial r D v^r}{\partial r} + \frac{\partial D v^z}{\partial z} = 0 , \tag{17}$$

$$\frac{\partial S^r}{\partial t} + \frac{1}{r}\frac{\partial r(S^r v^r + p)}{\partial r} + \frac{\partial S^r v^z}{\partial z} = \frac{p}{r} , \tag{18}$$

$$\frac{\partial S^z}{\partial t} + \frac{1}{r}\frac{\partial r S^z v^r}{\partial r} + \frac{\partial (S^z v^z + p)}{\partial z} = 0 , \tag{19}$$

$$\frac{\partial \tau}{\partial t} + \frac{1}{r}\frac{\partial r(S^r - D v^r)}{\partial r} + \frac{\partial (S^z - D v^z)}{\partial z} = 0 \tag{20}$$

or, in vector notation,

$$\frac{\partial \boldsymbol{U}}{\partial t} + \frac{1}{r}\frac{\partial r \boldsymbol{F}^r}{\partial r} + \frac{\partial \boldsymbol{F}^z}{\partial z} = \boldsymbol{S} , \tag{21}$$

with the vector of unknowns

$$\boldsymbol{U} = (D, S^r, S^z, \tau)^T , \tag{22}$$

fluxes,

$$\boldsymbol{F}^r = (D v^r, S^r v^r + p, S^z v^r, S^r - D v^r)^T , \tag{23}$$

$$\boldsymbol{F}^z = (D v^z, S^r v^z, S^z v^z + p, S^z - D v^z)^T , \tag{24}$$

and sources

$$\boldsymbol{S} = (0,\ p/r,\ 0,\ 0)^T\ . \tag{25}$$

An equation of state has to be supplied to close the system of equation (21). In our calculations we have assumed an ideal gas equation of state,

$$p = (\gamma - 1)\rho\epsilon\ , \tag{26}$$

where $4/3 \leq \gamma \leq 5/3$ is the (constant) adiabatic index of both the jet and the external medium fluids. A very important quantity derived from the equation of state is the local sound speed, c_s, which in the case of an ideal gas is given by

$$c_s^2 = \frac{\gamma(\gamma - 1)\epsilon}{1 + \gamma\epsilon}\ . \tag{27}$$

In our calculations, the system of equation (21) is solved on a discrete numerical grid. The time variation of the state vector $\boldsymbol{U}$ within a numerical cell is calculated by considering the fluxes across the cell interfaces of that cell. Using a method of lines, our discretization reads

$$\frac{d\boldsymbol{U}_{i,j}}{dt} = -\frac{1}{r_i \Delta r}\left(r_{i+(1/2)}\hat{\boldsymbol{F}}^r_{i+(1/2),j} - r_{i-(1/2)}\hat{\boldsymbol{F}}^r_{i-(1/2),j}\right) - \frac{1}{\Delta z}\left(\hat{\boldsymbol{F}}^z_{i,j+(1/2)} - \hat{\boldsymbol{F}}^z_{i,j-(1/2)}\right) + \boldsymbol{S}_{i,j}\ , \tag{28}$$

where the subscripts i and j refer to the r- and z-discretizations, respectively. $\boldsymbol{U}_{i,j}$ and $\boldsymbol{S}_{i,j}$ are the mean values of the state and the source vectors in the corresponding two-dimensional cell, while $\hat{\boldsymbol{F}}^r_{i+(1/2),j}$ and $\hat{\boldsymbol{F}}^z_{i,j+(1/2)}$ are the numerical fluxes at the cell interfaces. The latter are calculated with an approximate Riemann solver that uses the complete characteristic information contained in the Riemann problems between adjacent cells (Donat & Marquina 1996). It is based on the spectral decomposition of the Jacobian matrices of the relativistic system of equations derived by Font et al. (1994). The spatial accuracy of the algorithm is improved up to second order by means of a conservative monotonic parabolic reconstruction of the pressure, proper rest-mass density, and flow velocity following the work of Colella & Woodward (1984; see Martí & Müller 1996 for the explicit formulae used in our relativistic code). Integration in time is performed simultaneously in both spatial directions by using a total variation diminishing Runge-Kutta scheme of high order (Shu & Osher 1988). Finally, a one-dimensional Newton-Raphson iteration is used to compute in each time step the primitive variables $\{\rho, \epsilon, p, v^r, v^z\}$ from the conserved ones (see Martí & Müller 1996 for details). Appendix B contains a set of one- and two-dimensional test problems solved successfully with our code.

Our two sets of simulations (see § 3.2) cover the evolution of relativistic jets propagating through a homogeneous ambient medium in a region extending 50 (25) initial beam radii, R_b, in the z-direction and $7R_b$ in the r-direction. The computational domain is covered by a uniform numerical grid consisting of 1000 (500) × 140 zones. This corresponds to a spatial resolution of 20 zones per beam radius. The beam fluid is injected into the grid parallel to the symmetry axis (i.e., the z-axis) through a nozzle at the bottom ($r = 0$) of the left boundary of the grid ($z = 0$), which is 20 zones wide.

We have used outflow boundary conditions at all boundaries except at the symmetry axis ($r = 0$ boundary), where reflection conditions have been imposed, and at the nozzle, where we used fixed inflow beam conditions. In the radial direction the numerical grid described in the previous paragraph was extended by 28 geometrically spaced zones covering a region from $r = 7R_b$ to $r = 10.5R_b$ in order to delay and weaken the effect of a partial reflection of the bow shock at the top boundary.

3.2. *Covered Parameter Space*

Table 1 lists the initial parameters of all jet models we have calculated in our study. We have restricted ourselves to pressure-matched jets. The set of models consists of seven major simulations, which cover the evolution of the jet until it has propagated to a distance of about $z_{\max} = 50R_b$. In all these "long" simulations, the initial density ratio was set to $\eta = 0.01$ in order to focus on the effects caused by a variation of the internal beam Mach number and the beam flow velocity, which govern the strength of the relativistic terms. Relativistic effects are important whenever large velocities ($W \gg 1$) and/or large specific internal energies ($h \gg 1$) are encountered in the flow. Moreover, for large specific internal energies the local sound speed defined in equation (27) approaches the limit

$$c_s^{\max} = \sqrt{\gamma - 1}\ , \tag{29}$$

and it is seen that once v_b is specified, the value of the internal beam Mach number must be larger than

$$M^{\min} = \frac{v_b}{\sqrt{\gamma - 1}}\ , \tag{30}$$

which is the minimum Mach number for a flow with adiabatic exponent γ moving at speed v_b. Beams with large specific internal energies are then obtained for values of M_b near $M^{\min}$. Hence we fix the value of the classical beam Mach number in the initial setup to control the strength of the thermodynamical relativistic effects of our models. The proper Mach number, $\mathcal{M} = WM_b/W_s$, where W_s is the Lorentz factor associated with the local sound speed (Königl 1980), which plays the role of the classical Mach

TABLE 1

INITIAL PARAMETERS OF THE DIFFERENT MODELS

Model	η	γ	v_b	M_b	$\mathcal{M}_b$	$z_{\max}$
A1.....	0.01	4/3	0.99	1.72	9.97	50
A2.....	0.01	4/3	0.999	1.74	31.86	50
a1	1	4/3	0.99	1.72	9.97	25
a2	0.1	4/3	0.99	1.72	9.97	25
B1.....	0.01	4/3	0.99	6.0	41.95	50
B2.....	0.01	4/3	0.999	6.0	132.32	50
b1	0.1	4/3	0.9	6.0	13.61	25
b2	0.1	4/3	0.99	6.0	41.95	25
C1.....	0.01	5/3	0.9	6.0	13.61	50
C2.....	0.01	5/3	0.99	6.0	41.95	50
C3.....	0.01	5/3	0.999	6.0	132.32	50
c1	0.1	5/3	0.9	6.0	13.61	25
c2	0.1	5/3	0.99	6.0	41.95	25

NOTE.—Here η is the ratio of the rest-mass density of the beam fluid and the ambient medium; γ is the adiabatic index; v_b is the beam velocity; M_b is the Mach number (Newtonian definition); $\mathcal{M}_b$ is the beam proper Mach number; $z_{\max}$ is the distance up to which the model has been evolved.

number in two-dimensional steady relativistic hydrodynamics, is also shown in Table 1.

The seven basis models of our sample have been chosen to study both types of relativistic effects and can be classified according to the following scheme:

L1. *Hot models* ($M_b \approx M^{\min}$).—A1 ($v_b = 0.99$) and A2 ($v_b = 0.999$). Relativistic effects from large beam internal energies are important and comparable to the effects from flow speeds near the speed of light.

L2. *Highly supersonic models* ($M_b \gg M^{\min}$):

(*a*) *Models with* $\gamma = 4/3$.—B1 ($v_b = 0.99$) and B2 ($v_b = 0.999$);

(*b*) *Models with* $\gamma = 5/3$.—C1 ($v_b = 0.9$), C2 ($v_b = 0.99$), and C3 ($v_b = 0.999$).

Here relativistic effects from large beam speeds dominate.

According to this classification, the relativistic jet models considered by Martí et al. (1994) and Duncan & Hughes (1994) all are hot models.

Figures 1*a*–1*g* (Plates 1–4) show the density and pressure distribution and the flow velocity vectors of these seven models at the end of the simulation, when the leading bow shock is about to leave the computational domain.

The beam, the cocoon (blue/red region surrounding the beam in the density frames), and the bow shock can be clearly identified in all figures. Figures 1*a*–1*g* confirm the morphological considerations discussed at the beginning of this section. The hot models A1 (Fig. 1*a*) and A2 (Fig. 1*b*) possess very thin cocoons while the highly supersonic models C1, C2, and C3 (Figs. 1*e*–1*g*) are dominated by a thick cocoon that tends to become less prominent as the beam Lorentz factor increases. The most outstanding property of models B1 and B2 (Figs. 1*c* and 1*d*) is their extremely narrow bow shock, which is the result of the acceleration of the jet (see below).

The basis set of "long" simulations has been supplemented with a subset of six models, which have a larger initial density ratio ($\eta = 0.1$ and $\eta = 1.0$) but which have been evolved only half as far in length ($z_{\max} = 25R_b$). Models a1 and a2 form, together with model A1, a sequence of low beam Mach number jets with a relativistic beam flow velocity and a decreasing initial density contrast (from $\eta = 1.0$ to $\eta = 0.01$). The initial conditions of models c1, c2, and b2 are the same as those of models C1, C2, and B1, respectively, except for a larger value of the density contrast ($\eta = 0.1$ instead of $\eta = 0.01$). Finally, model b1 is almost identical to model b2 except for its smaller value of the beam flow velocity ($v_b = 0.9$ instead of $v_b = 0.99$).

In the remainder of the section, we present the morphological and dynamical properties of our models in detail. The structural features of the jets, i.e., head, cocoon, and beam, are discussed in different subsections although their properties are closely related to each other. In the discussion we shall use models A1, B1, and C2 as prototypes and refer to the other models whenever it is appropriate.

3.3. *Structure and Dynamics of the Head of the Jet*

As in classical jets (see, e.g., Norman et al. 1982), the head of a relativistic jet consists of a terminal shock (a Mach shock) where the beam fluid is decelerated, converting its bulk kinetic energy into internal energy, a contact discontinuity (the working surface) that separates the beam fluid from the ambient medium, and a bow shock. The motion of the working surface determines the propagation speed of the jet through its environment.

Figures 2*a*, 3*a*, and 4*a* (Plates 5, 7, and 9) show the logarithm of the rest-mass density for a sequence of snapshots of models A1, B1, and C2, respectively. Obviously, models with low and high beam Mach numbers exhibit very different behavior. Whereas in the first case (model A1) the Mach shock is well defined during the whole simulation, it is occasionally substituted by cross shocks in the high beam Mach number models B1 and C2. Moreover, as these oblique shocks are less efficient than normal shocks in decelerating the beam flow, the contact discontinuity is easily perturbed in these highly supersonic models. The perturbation of the contact discontinuity, already found in classical jets with high beam Mach number (see Norman et al. 1982; Kössl & Müller 1988), is responsible for the production of the vortices seen at the working surface in Figures 3*a* and 4*a*.

For highly supersonic jets with $\gamma = 4/3$, i.e., models of category L2*a*, the contact discontinuity is close to the bow shock. This gives rise to bow shock perturbations, causing changes in its overall shape, which are reminiscent of the "nose cones" observed in classical MHD jets (Clarke et al. 1989; Lind et al. 1989). In model B1 (Fig. 3), for example, a first change in the shape of the bow shock begins to develop in Figure 3*a*, frame (d), when the original Mach disk disappears. A similar behavior is seen in Figure 3*a*, frame (l), just at the end of our simulation. The perturbations of the bow shock are connected with an increase of the propagation velocity of the jet through the external medium. The acceleration of the jet is caused by the reconfinement effect of the internal shocks, which reduce the effective section of the beam and thus increase the momentum transferred per unit area. This behavior is also observed in models B2, b1, and b2. As the distance of the first conical shock from the source grows with the beam flow velocity, the change in shape of the bow shock occurs nearer to the source in model b1 (at about $10R_b$) than in model B1 ($22R_b$), and further away in model B2 ($30R_b$). Whether this is a recurrent process by which the beam itself is becoming narrower or whether it is only a "readjustment" of the jet to the initial conditions cannot be concluded from our present simulations. We point out, however, that a similar behavior, which was clearly recurrent, has been found in the long-term simulations of extremely supersonic classical jets performed by Massaglia et al. (1996).

On the other hand, in the case of model A1 (Fig. 2), we observe an almost steady beam flow near the head, which makes the jet head very stable. This result holds for model A2 (cf. Figs. 1*a* and 1*b*), too. It seems to be a generic property of hot jets, because it is also found in models a2 ($\eta = 0.1$) and a1 ($\eta = 1.0$).

3.4. *Cocoon Structure and Backflow Dynamics*

We find a strong dependence of the structure of the cocoon upon the beam Mach number (see Figs. 2*a*, 3*a*, and 4*a*). Structural differences in the cocoon morphology are already evident at the beginning of the evolution (cf., for instance, frame [a] in Figs. 2*a*, 3*a*, and 4*a*). Relativistic beams with internal Mach numbers close to the minimum value are surrounded by lobes instead of cocoons. This result, which was already found by Martí et al. (1994), is in agreement with our theoretical prediction that cocoons are not prominent in hot jets. Moreover, in our relativistic

models the absence of vortex shedding by the head produces a very stable structure. Consequently, in these jets the backflow is minimized, too. It is either restricted to a small region near the head, as in models A1 (see flow velocity panel in Fig. 1*a*), a1, and a2, or does not exist at all, as in model A2 (Fig. 1*b*).

Backflow is more important in jets with a high beam Mach number, where stable cocoons are found in the early stages of the evolution. The cocoons eventually evolve into vortices, producing turbulent structures (Fig. 3*a*, model B1; Fig. 4*a*, model C2; see also models B2, C1, and C3). New vortices are continuously produced by the head of the jet as a result of its nonsteady propagation. The vortices grow as they are advected upstream.

We find that the cocoon structure varies with the value of the adiabatic exponent. For models with $\gamma = 5/3$, the cocoon is mainly formed by large vortices. At the end of the simulation, the cocoon has an almost constant thickness along the beam ($\sim 4R_b$ for model C2, and $\sim 3R_b$ for model C3). For models with $\gamma = 4/3$, the strong beam collimation resulting from the first internal conical shock causes a large acceleration of the jet. During the acceleration phase (around frame [d] in Fig. 3*a*), the beam gas is less efficiently redirected into the cocoon. After the acceleration phase (frame [e] and later), the continuous flow into the cocoon is reestablished, but it is very weak and has difficulties propagating upstream. Hence small, turbulent vortices form very soon. The transition between the parts of the cocoon formed before and after the acceleration is seen in the cocoon structure around $z \approx (15\text{–}18)R_b$ (see frames [e]–[l] in Fig. 3*a*).

The absence of extended cocoons in models with small internal beam Mach numbers causes the jet to evolve such that the beam gas is in pressure equilibrium with the shocked ambient gas (except for a region near the head of the jet). This is seen in Figure 2*b* (Plate 6), where we plot an evolutionary sequence of the pressure distribution of model A1. Similar plots for models B1 and C2 are shown in Figures 3*b* and 4*b* (Plates 8 and 10), respectively. The lack of internal structure found in the hot jets is probably a consequence of the pressure equilibrium (see § 3.5). Highly supersonic jets, on the contrary, possess a rich internal structure and overpressured cocoons (Figs. 3*b* and 4*b*). The pressure distribution within the cocoon/shocked ambient medium is displayed in Figure 5 for models C1, C2, and C3, respectively. It shows the logarithm of the pressure normalized to the initial beam pressure as a function of radial distance for three values of the z-coordinate at the end of the simulations. From Figure 5, an interesting dependence of the mean pressure within the cocoon upon the bulk flow Lorentz factor in the beam can be obtained. The overpressure for models C1, C2, and C3 is approximately a factor of 3, 8, and 25, respectively, which is roughly proportional to the corresponding beam flow Lorentz factor (2.3, 7.1, and 22.2). The buildup of an overpressured cocoon was also discussed by Begelman & Cioffi (1989) and numerically explored and confirmed by Loken et al. (1992) for Newtonian hypersonic jets.

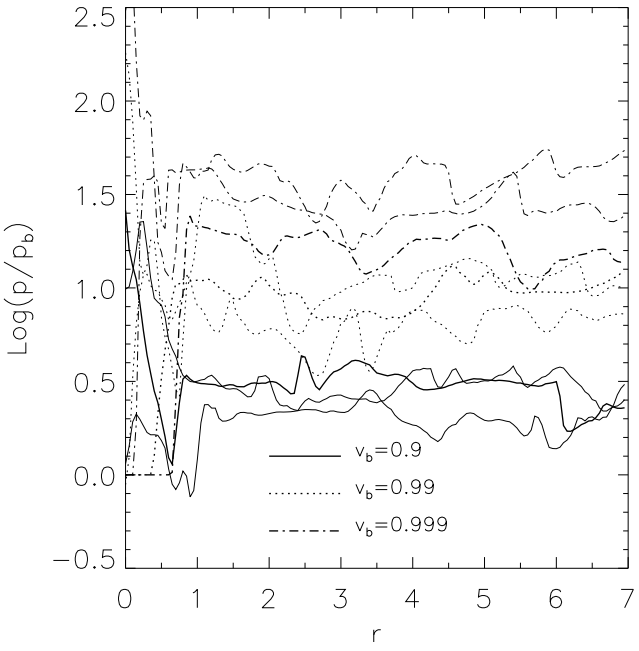

FIG. 5.—Logarithm of the pressure normalized to the initial beam pressure for models C1 (*solid line*), C2 (*dotted line*), and C3 (*dash-dotted line*) as a function of position along several lines perpendicular to the jet axis ($z \simeq 7$—*thickest line*—$z \simeq 17$, and $z \simeq 27$—*thinnest line*) at the end of the simulation (see Figs. 1*e*–1*g*). The pressure in the cocoon grows with the initial beam velocity.

3.5. *Beam*

The presence of shocks within the beam is directly connected with the structure of the cocoon and the dynamical processes occurring within it. Beams of relativistic, hot ($M_b \approx M_{\min}$) models of our sample (i.e., models A1, B2, a1, a2; see, e.g., Figs. 1*a*, 1*b*) have an almost complete lack of internal structure, in agreement with previous simulations (Martí et al. 1994; Duncan & Hughes 1994). The absence of shocks in hot beams is a consequence of the pressure equilibrium between the beam and the surrounding cocoon/shocked ambient medium. It also reflects the great stability of the beam surface against the growth of pinch instabilities (the most disruptive modes in cylindrically symmetric flows), which would cause internal shocks as in classical jets. Neither the reflecting mode nor the fundamental, or ordinary, pinch mode (typical of low beam Mach number flows; see Norman et al. 1984 and references cited therein) seems to develop in these hot jets (at least for the timescales covered by our study). The effect of an instability dominated by the fundamental mode is to create an ever broadening mixing layer that eventually would destroy the supersonic beam. We have performed three simulations with $M_b = 1.72$ and density ratios of 0.01, 0.1, and 1.0, respectively. In all three cases we have obtained naked beams, but no trace of growing pinch modes has been detected. This result is consistent with the study of Kelvin-Helmholtz instabilities in the linear regime performed by Ferrari, Trussoni, & Zaninetti (1978), who found relativistic, hot jets to be unconditionally stable.

Models having a high beam Mach number display, on the contrary, a very rich and complex structure within the beam. Internal oblique shocks separating compressed and rarefied regions are found. The reconfining effect of these internal shocks is evident in the flow velocity panels of Figure 1, although it is more important in models with larger beam velocity and smaller adiabatic exponent (e.g., models B1 and B2). In these highly supersonic models, internal structure is generated within the beam by perturbations of the beam boundary by vortices and bulk motions

TABLE 2

PROPAGATION PROPERTIES OF RELATIVISTIC JETS

Model	ϵ_b	V_j^N	V_j^R	$\bar{v}_h$	δ
A. Hot Relativistic Jets					
a1	1.23×10^2	0.50	0.87	0.85	0.98
a2	1.23×10^2	0.24	0.86	0.85	0.99
A1.....	1.23×10^2	0.09	0.84	0.86	1.02
A2.....	6.61×10^1	0.09	0.94	0.93	0.99
B. Highly Supersonic Relativistic Jets ($\gamma = 4/3$)					
b1	5.43×10^{-2}	0.22	0.39	0.43	1.10
b2	6.67×10^{-2}	0.24	0.69	0.73	1.06
B1.....	6.67×10^{-2}	0.09	0.42	0.52	1.24
B2.....	6.80×10^{-2}	0.09	0.70	0.80	1.14
C. Highly Supersonic Relativistic Jets ($\gamma = 5/3$)					
c1	2.09×10^{-2}	0.22	0.38	0.39	1.03
c2	2.55×10^{-2}	0.24	0.69	0.71	1.03
C1.....	2.09×10^{-2}	0.08	0.17	0.13	0.76
C2.....	2.55×10^{-2}	0.09	0.42	0.37	0.88
C3.....	2.60×10^{-2}	0.09	0.69	0.67	0.97

NOTE.—Here ϵ_b is the beam specific internal energy, V_j^N and V_j^R are respectively the Newtonian and relativistic one-dimensional estimates of the velocity of the jet, $\bar{v}_h$ is the numerically obtained average velocity of the head of the jet, and δ is the propagation efficiency of the jet.

within the cocoon. Additional internal structure (such as the oblique shock created at the edge of the nozzle) is formed by pressure mismatches between the beam and the high-pressure cocoon. The angle formed by these oblique shocks with the jet axis decreases with the proper beam Mach number. In particular, we find from our simulations that the conical shock impinges the axis at increasingly larger distances along the sequence of models C1, C2, and C3 (at $7R_b$, $10R_b$, and $20R_b$, respectively), as well as along the model sequence B1 and B2 ($22R_b$ and $30R_b$, respectively). Because of the small angle between the first conical shock in models B1 and B2 and the direction of the beam flow, these shocks are extremely inefficient in decelerating the beam material and are, hence, responsible for the observed acceleration of the jet head in these models.

3.6. *Propagation Efficiency*

As for classical jets (see, e.g., Norman et al. 1983), we define the propagation efficiency of jets, δ, as the ratio between the average propagation velocity, $\bar{v}_h$, of the head of the jet and its corresponding one-dimensional estimate, V_j^R, given by equation (5):

$$\delta = \bar{v}_j / V_j^R \, . \tag{31}$$

Our results show (see Table 2) that, for a wide range of estimated jet propagation speeds ($0.17 \leq V_j^R \leq 0.94$), the efficiencies span the interval 0.76–1.24. These high efficiencies, in particular those greater than 1.0, significantly exceed those obtained for Newtonian jets. Norman et al. (1983) found $0.49 \leq \delta \leq 0.90$ for their comprehensive set of jet models including diffuse and dense jets, as well as highly supersonic ones ($M_b \leq 12$). The efficiencies of our models are only comparable with the hypersonic Newtonian models ($M_b \approx 30$–300) computed by Massaglia et al. (1996).

Efficiencies very close to unity (i.e., 1.00 ± 0.02) are obtained for our subsample of hot models (a1, a2, A1, A2; see Table 2A). The lack of internal structure within the beam and the not very prominent or nonexistent cocoon are responsible for the almost one-dimensional behavior of these jets. Models that are highly supersonic and have a small adiabatic index ($\gamma = 4/3$) have efficiencies greater than 100% (b1, b2, B1, B2; see Table 2B). This remarkable result is caused by an acceleration of those jets during an early stage of their evolution, after the first oblique internal shock has formed within the beam. The acceleration of the jet is seen in Figure 3*a* through the change of shape of the bow

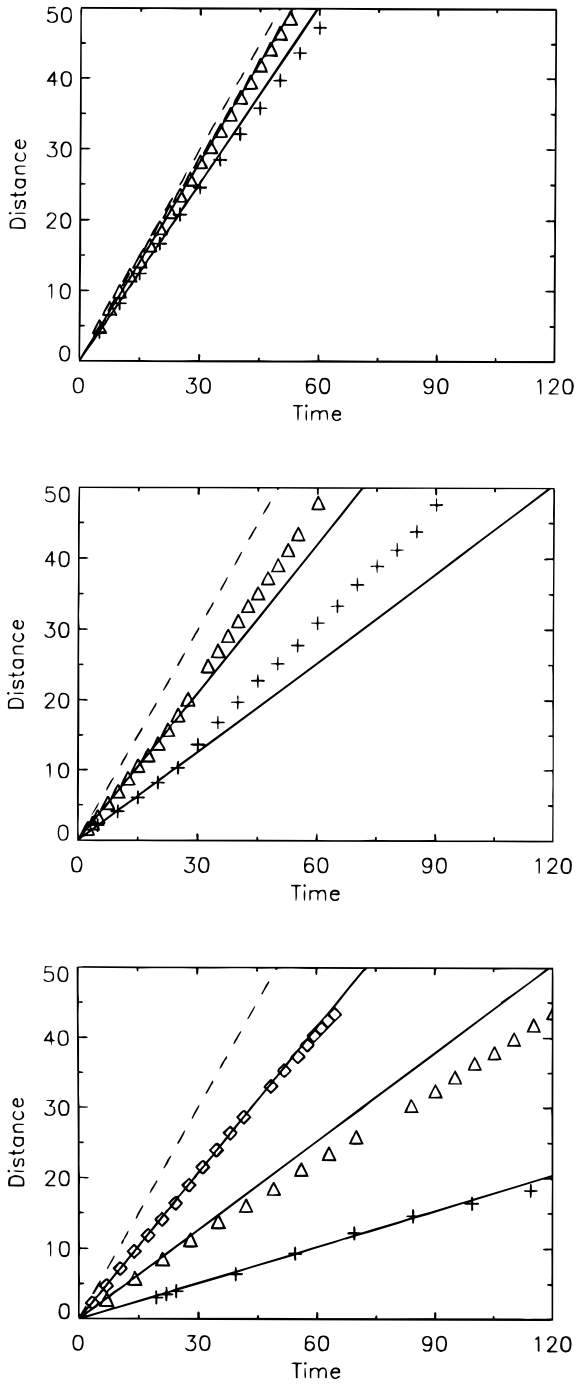

FIG. 6.—Position of the jet head as a function of time for models A1 (*plus signs*) and A2 (*triangles*) (*top*), models B1 (*plus signs*) and B2 (*triangles*) (*middle*), and models C1 (*plus signs*), C2 (*triangles*), and C3 (*diamonds*) (*bottom*). Solid lines correspond to the theoretical estimates calculated through eq. (22). The dashed line corresponds to a hypothetical jet propagation velocity equal to the speed of light.

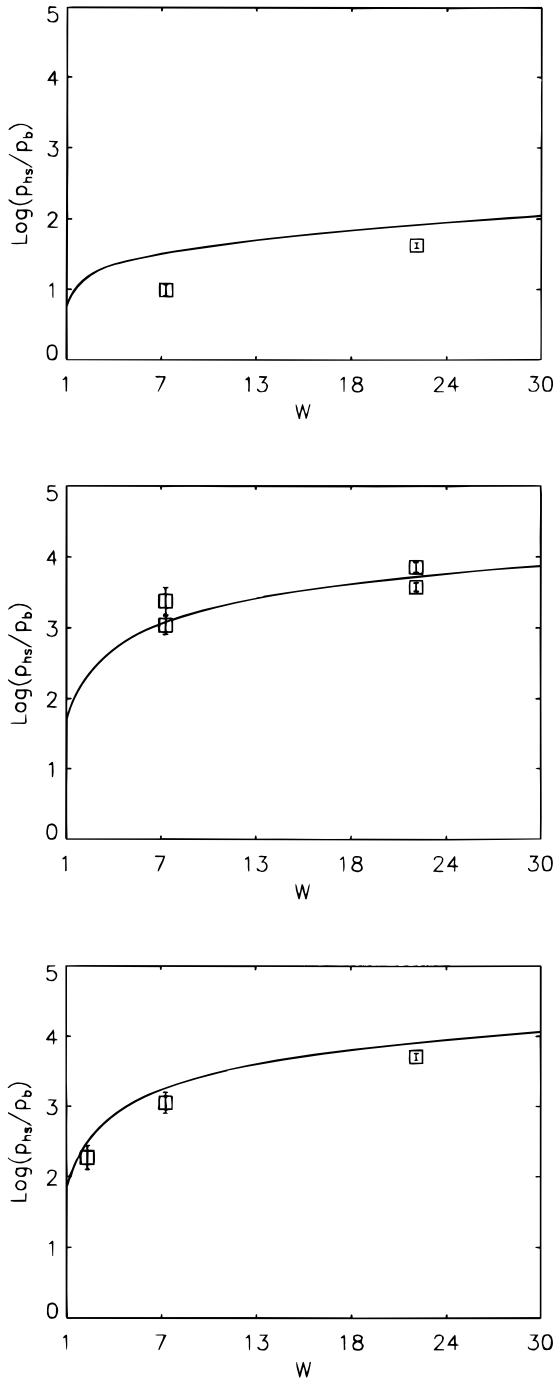

FIG. 7.—Logarithm of the pressure in the hot spot, normalized to the initial beam pressure, as a function of the beam Lorentz factor. The solid line represents the logarithm of the pressure at the hot spot, assuming pure one-dimensional momentum transfer. The squares represent the time-averaged hot-spot pressures of models A1 ($W = 7.09$) and A2 ($W = 22.37$) (*top*), B1 ($W = 7.09$) and B2 ($W = 22.37$) (*middle*), and C1 ($W = 2.29$), C2 ($W = 7.09$), and C3 ($W = 22.37$) (*bottom*). The error bars correspond to one standard deviation from the mean. In the middle panel, lower time-averaged values correspond to the evolution prior to the jet acceleration ($t < 25$ for model B1; $t < 30$ for model B2). Upper time-averaged values correspond to the evolution after the acceleration phase.

shock between frames (c) and (e). This process happens again later (see frame [l]) after a second oblique shock is created in the beam. Finally, according to the data shown in Table 2C, we can conclude that the efficiency of models that are highly supersonic and have a large adiabatic index ($\gamma = 5/3$; subset L2*b*) increases with η for fixed v_b (compare models c1 and C1, or c2 and C2), with v_b for fixed and small η (compare models C1, C2, and C3), and tends to 100% for sufficiently dense, highly relativistic models (see models c1 and c2).

In Figure 6, the distance traveled by the head of the jet is shown as a function of time for models A, B, and C. The solid lines represent the predicted position of the jet head according to the one-dimensional relativistic estimate. The dashed line corresponds to a propagation velocity equal to the speed of light. The symbols in each panel mark the position of the head for a selected set of time steps for each model. In the case of models A and C, the head propagates slower than predicted by the one-dimensional estimate. On the other hand, for models B1 and B2 the head moves at the estimated speed early on in the evolution ($t < 25$ in model B1; $t < 30$ in model B2) and then accelerates. In both models, B1 and B2, the position of the head at the end of the simulation (rightmost symbols in Fig. 6, *middle*) is consistent with the onset of another acceleration phase. Besides these two acceleration phases, there is no indication in our results of any other significant instantaneous acceleration taking place during the evolution of the jets.

4. DISCUSSION AND CONCLUSIONS

The most remarkable result of our comprehensive study of relativistic jets is definitely the large propagation speed of the jets compared to the corresponding Newtonian models. It is also important to note that the one-dimensional estimate for the propagation speed based on a simple momentum balance argument is extremely well confirmed by the two-dimensional hydrodynamic simulations. The large propagation speed causes the cocoons of relativistic jets to be generally less prominent than those of Newtonian jets. This morphological characteristic is distinctly exhibited by models of type A, which consist of an almost featureless beam surrounded by a very thin cocoon extending back from the head of the jet about halfway to the nozzle. As illustrated by the sequence of models C1, C2, and C3, the cocoon thickness decreases with increasing beam flow velocity, which coincides with an increase of the propagation efficiency of the jet.

In the case of L1 models, the jet propagation velocities are so large (0.85–0.93) and the backflow within the thin cocoon so unimportant that the jet is unable to produce an extended cocoon. Matter deflected at the working surface remains near the head of the jet, forming a kind of lobe. In L2 models, the jets have extended overpressured cocoons, the mean pressure increasing almost proportionally to the beam Lorentz factor. The existence of overpressured cocoons was also pointed out by Begelman & Cioffi (1989) and confirmed by Loken et al. (1992) for Newtonian hypersonic jets (see also Massaglia et al. 1996). These overpressured cocoons could help to confine the jets during their early evolution and might be of relevance for the formation of knots often observed in large-scale jets of powerful radio sources.

Qualitatively speaking, the results obtained in our simulations of relativistic jets are consistent with the properties of very dense Newtonian jets. This fact can easily be explained by considering that both the specific enthalpy (in hot jets) and the Lorentz factor (in highly supersonic jets) increase the effective inertial mass of the beam. The enhanced inertia, which directly follows from the momen-

tum equation, makes it more difficult to perturb relativistic jets than Newtonian ones. It is also the reason that the one-dimensional propagation estimates agree so well with the numerical results. The "one-dimensionality" of relativistic jets is further supported by comparing the (time-averaged) pressure at the working surface near the jet axis with the pressure predicted in the corresponding one-dimensional problem. This problem of the impact of a one-dimensional high-speed flow on a homogeneous ambient medium at rest can be solved analytically by using the analytical solution of the relativistic Riemann problem derived by Martí & Müller (1994). Applying this procedure to the initial setups of our models, one can derive bounds for the thermal pressure at the point of impact at the head of the jet. The resulting pressure, normalized to the beam pressure, is plotted in Figure 7 for model types L1, L2*a*, and L2*b*. The solid line in Figure 7, which shows the logarithm of the thermal pressure at the point of impact (in units of the beam pressure) as a function of the beam flow velocity, indicates that a larger impact velocity gives rise to a larger pressure. Figure 7 further illustrates that the numerically obtained time-averaged pressure at the head of the jet (the error bars correspond to one standard deviation) agrees quite well with the one-dimensional estimate for all models. The noticeable decrease of the size of the error bars (i.e., decreasing deviations from the mean pressure value) with increasing beam flow velocity seen in Figure 7 once more confirms the stability of relativistic flows against perturbations.

As a general conclusion, we can say that relativistic jets seem to have very promising properties to propagate large distances without being destabilized or even disrupted, which is required for a successful modeling of observed jets in extragalactic radio sources. However, realistic simulations have to be extended to much larger distances in order to account for the expected deceleration between parsec and kiloparsec scales. The simulations of relativistic jets have also to be performed in three spatial dimensions to check for the development of possible nonaxisymmetric perturbations (see Hardee, Clarke, & Howell 1995).

The authors want to thank the anonymous referee for instructive comments that helped to improve the paper. J. M[a]. M. is indebted to the Max-Planck-Institut für Astrophysik, where most of the work was carried out, for the kind hospitality during his stay. He also acknowledges financial support from the Commission of the European Communities through its Human Capital and Mobility Program (contract ERBCHBICT930496) and the Spanish Ministerio de Educación. This research has been supported in part by the Spanish DGICYT (PB94-0973, PB94-0987).

APPENDIX A

THE APPROXIMATE RIEMANN SOLVER

The numerical simulations presented in this paper have been performed using an approximate Riemann solver, proposed in Donat & Marquina (1996), due to Marquina. Marquina's flux formula introduces a dissipative mechanism into the numerical scheme especially designed to eliminate undesired pathologies (such as the overheating phenomenon in wall shock reflection experiments or the long-wavelength noise behind slowly moving shocks; see Donat & Marquina 1996), which flaw most high-order shock-capturing methods, if no excessive smearing is introduced at discontinuities. Contrary to other linearized solvers (e.g., Roe 1981), Marquina's Riemann solver is not based on averaging's being able to solve Riemann problems with different left and right equations of state. It has been designed for general hyperbolic systems of conservation laws and, in the case of relativistic fluid dynamics, has allowed us to reach the ultrarelativistic limit with great accuracy (see Appendix B). Moreover, our experimentation confirms that in two dimensions the dissipation of the scheme is sufficient to eliminate the carbuncle phenomenon (see, e.g., Quirk 1994), which appears in all our high Mach number relativistic jet simulations when using other standard solvers.

Marquina's flux formula applied to a system of conservation laws in one dimension,

$$\frac{\partial \boldsymbol{U}}{\partial t} + \frac{\partial \boldsymbol{F}(\boldsymbol{U})}{\partial x} = 0 \,, \tag{A1}$$

yields a conservative method whose numerical flux function is computed as follows: Given left and right states, the "*sided*" local characteristic variables and fluxes are calculated according to

$$\omega_l^p = \boldsymbol{l}^p(\boldsymbol{U}_l) \cdot \boldsymbol{U}_l \,, \qquad \phi_l^p = \boldsymbol{l}^p(\boldsymbol{U}_l) \cdot \boldsymbol{F}(\boldsymbol{U}_l) \,,$$
$$\omega_r^p = \boldsymbol{l}^p(\boldsymbol{U}_r) \cdot \boldsymbol{U}_r \,, \qquad \phi_r^p = \boldsymbol{l}^p(\boldsymbol{U}_r) \cdot \boldsymbol{F}(\boldsymbol{U}_r) \,,$$

for $p = 1, 2, \ldots, m$, where m is the number of equations of the system. Here $\boldsymbol{l}^p(\boldsymbol{U}_l)$ and $\boldsymbol{l}^p(\boldsymbol{U}_r)$, are the (normalized) left eigenvectors of the Jacobian matrix of the system of equation (A1), $\mathbf{A}$, calculated in the left and right states, $\boldsymbol{U}_l$ and $\boldsymbol{U}_r$.

Let $\lambda_1(\boldsymbol{U}_l), \ldots, \lambda_m(\boldsymbol{U}_l)$ and $\lambda_1(\boldsymbol{U}_r), \ldots, \lambda_m(\boldsymbol{U}_r)$ be the corresponding eigenvalues. Then, for every $k = 1, \ldots, m$, we proceed as follows:

1. If $\lambda_k(\boldsymbol{U})$ does not change sign in $[\boldsymbol{U}_l, \boldsymbol{U}_r]$ [for the equations of fluid dynamics, if $\lambda_k(\boldsymbol{U}_l) \cdot \lambda_k(\boldsymbol{U}_r) > 0$], then the scalar scheme is upwind and the numerical flux is calculated according to the relevant characteristic information:

If $\lambda_k(\boldsymbol{U}_l) > 0$, then

$$\phi_+^k = \phi_l^k \,, \qquad \phi_-^k = 0 \,,$$

else

$$\phi_+^k = 0 \,, \qquad \phi_-^k = \phi_r^k \,.$$

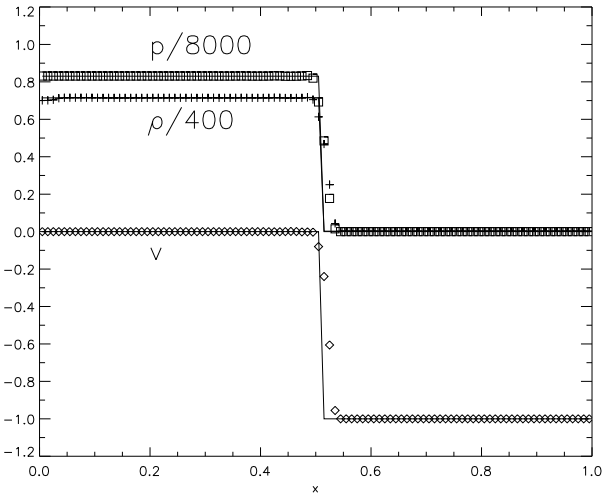

FIG. 8*a*

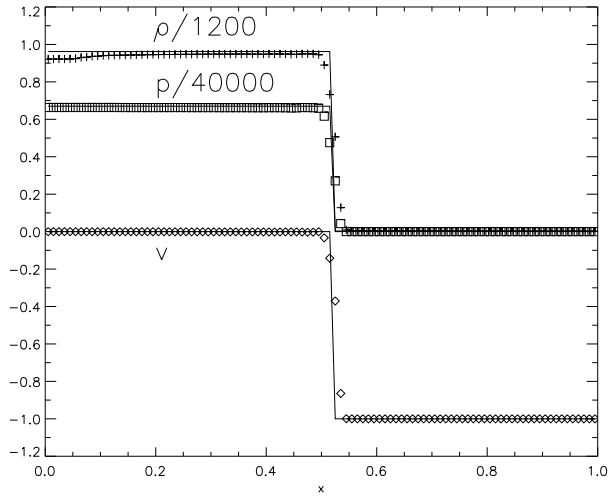

FIG. 8*b*

FIG. 8.—(*a*) Exact (*solid lines*) and numerical profiles of pressure, density, and flow velocity for the planar shock reflection problem with an inflow velocity $v_1 = -0.9999$, when the shock has propagated 50 zones off the site of reflection (at $x = 0$). The computations were performed on a uniform grid of 100 zones. (*b*) Same as (*a*), but for the cylindrical shock reflection problem.

2. Otherwise, as a way to avoid the aforementioned numerical pathologies, the scalar scheme is switched to the more viscous, entropy-satisfying local Lax-Friedrichs scheme:

$$\alpha_k = \max \{|\lambda_k(\boldsymbol{U}_l)|, |\lambda_k(\boldsymbol{U}_r)|\} ,$$
$$\phi^k_+ = (\phi^k_l + \alpha_k \omega^k_l)/2 , \qquad \phi^k_- = (\phi^k_r - \alpha_k \omega^k_r)/2$$

(see Donat & Marquina 1996 for details).

Marquina's flux formula is then

$$\hat{\boldsymbol{F}}^{\mathrm{M}}(\boldsymbol{U}_l, \boldsymbol{U}_r) = \sum_{p=1}^{m} [\phi^p_+ \boldsymbol{r}^p(\boldsymbol{U}_l) + \phi^p_- \boldsymbol{r}^p(\boldsymbol{U}_r)] , \tag{A2}$$

where $\boldsymbol{r}^p(\boldsymbol{U}_l)$, $\boldsymbol{r}^p(\boldsymbol{U}_r)$ are the right (normalized) eigenvectors of the Jacobian matrices $\mathbf{A}(\boldsymbol{U}_l)$, $\mathbf{A}(\boldsymbol{U}_r)$.

The spectral decomposition of the Jacobian matrices associated to the equations of relativistic hydrodynamics can be found in Font et al. (1994). In our calculations, the numerical fluxes are computed by using equation (A2), taking as left and right states the reconstructed values at the interfaces.

Marquina's numerical flux is consistent, i.e., $\hat{\boldsymbol{F}}^{\mathrm{M}}(\boldsymbol{U}, \boldsymbol{U}) = \boldsymbol{F}(\boldsymbol{U})$, implying local convergence of the numerical scheme, and in fact, when applied to a constant-coefficient one-dimensional system, Marquina's scheme yields the exact solution to the Riemann problem.

APPENDIX B

ONE- AND TWO-DIMENSIONAL TEST PROBLEMS

We have tested our code against several problems involving strong shocks and high Lorentz factor flows, which have an analytical solution.

B1. PLANAR AND CYLINDRICAL RELATIVISTIC SHOCK REFLECTION

We first consider the one-dimensional problem of the reflection of a shock wave assuming planar, axial, or spherical symmetry. Initially, i.e., at $t = 0$, we have an inflowing cold (i.e., $\epsilon = 0$) gas with coordinate velocity v_1 and Lorentz factor W_1, which fills the computational domain. In the case of planar symmetry, the gas is supposed to hit a wall placed at one of the edges of the grid while, in the cases of cylindrical and spherical symmetry, the gas converges toward the axis or the center of symmetry, respectively. In all three cases the reflection causes compression and heating of the gas as kinetic energy is converted into internal energy. This occurs in a shock wave, which propagates upstream. Behind the shock the gas is at rest ($v_2 = 0$), and as a consequence of conservation of energy across the shock, the gas has a specific internal energy given by

$$\epsilon_2 = W_1 - 1 .$$

The compression ratio between shocked and unshocked gas, $\sigma = \rho_2/\rho_1$, follows from

$$\sigma = \frac{\gamma + 1}{\gamma - 1} + \frac{\gamma}{\gamma - 1} \epsilon_2 ,$$

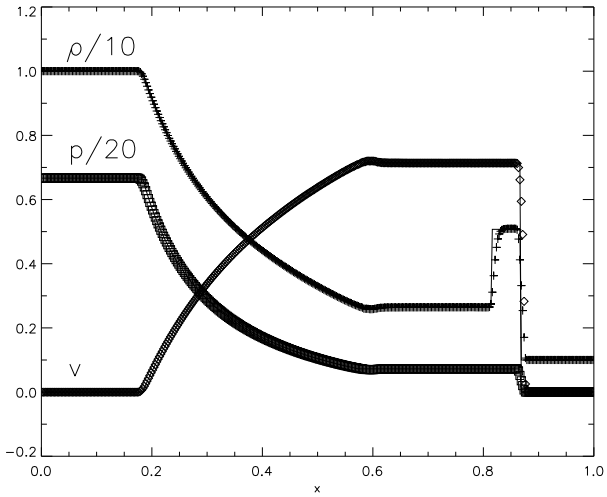

FIG. 9.—Exact (*solid lines*) and numerical profiles of pressure, density, and flow velocity of the one-dimensional relativistic shock tube. The computations were performed on a uniform grid of 400 zones.

where γ is the adiabatic index of the equation of state. The shock velocity is given by

$$V_s = \frac{(\gamma - 1)W_1 |v_1|}{W_1 + 1} .$$

In the unshocked region ($r \in [V_s t, \infty]$), the pressureless gas flow is self-similar and has a density distribution given by

$$\rho_1 = \left(1 + \frac{v_1 t}{r}\right)^{\alpha} \rho_0 ,$$

where $\alpha = 0, 1, 2$ for planar, cylindrical, or spherical symmetry, respectively, and where ρ_0 is the density of the inflowing gas at infinity.

In our test calculations, we have used a gas with an adiabatic index $\gamma = 4/3$ and an inflow velocity $v_1 = -0.9999$, corresponding to a Lorentz factor $W_1 = 70.9$. The computational grid consisted of 100 uniform zones covering the interval $r \in [0, 1]$ and the reflection, occurring at $r = 0$. For numerical reasons the specific internal energy of the inflowing gas was set to a small finite value ($\epsilon = 10^{-5} W_1$) and the density at infinity was set equal to 1.

Figures 8*a* and 8*b* show the profiles of pressure, rest-mass density, and flow velocity for planar and cylindrical shock reflection, respectively. The profiles are shown after the shock has propagated 50 zones off the site of reflection. In both cases the shock wave is resolved by three zones, and there are no postshock numerical oscillations. The density jumps by a factor of ≈ 400 across the shock. Near $r = 0$, the density distribution slightly undershoots the analytical solution ($\approx 1\%$ in the planar and $\approx 4\%$ in the cylindrical case) as a result of the numerical effect of wall heating. In the cylindrical case, an additional systematic error of $\approx 1\%$ in the postshock density occurs.

B2. ONE-DIMENSIONAL RELATIVISTIC SHOCK TUBE

Shock tubes represent a special case of a Riemann problem, in which the fluid in the states on both sides of the discontinuity is at rest. They provide a useful tool to test numerical codes, because their evolution involves shock waves and rarefactions and because analytical solutions are known. We have simulated several shock-tube problems with large jumps in the initial pressure distribution, developing strong shocks that propagate at relativistic speeds. The numerical solutions obtained with our hydrocode are stable (provided the Courant condition is fulfilled) and converge when the grid is refined. As an example, we show here the results obtained for a particular problem characterized by the following initial state:

$$\rho_L = 10.0 , \quad \rho_R = 1.0 ; \qquad p_L = 13.3 , \quad p_R = 6.610^{-7} ; \qquad v_L = v_R = 0 ; \qquad \gamma_L = \gamma_R = 5/3 .$$

The analytical solution can be obtained by using the procedure described in Martí & Müller (1994). The decay of the initial discontinuity gives rise to an intermediate state located between a shock wave and a transonic rarefaction propagating to the right. In this intermediate state, the fluid moves to the right at a speed of 0.72 behind the shock, whose speed is 0.83. The density jump across the shock is equal to 5.1, which is larger than the classical limit of 4.0 for strong shocks (for $\gamma = 5/3$). A contact discontinuity divides the intermediate state into two regions that have different rest-mass densities.

We have performed this test with a one-dimensional version of our hydrocode, using a uniform grid of 400 zones. The initial discontinuity was located in the middle of the grid covering the interval $x \in [0, 1]$. Figure 9 shows the resulting distributions of pressure, density, and fluid flow velocity. The numerical solution is free of spurious oscillations. The shock is smeared across five zones while the contact discontinuity (see the rest-mass density profile) is broadened somewhat more by numerical diffusion. The constant states and the transition state across the rarefaction are captured with errors smaller than 1%.

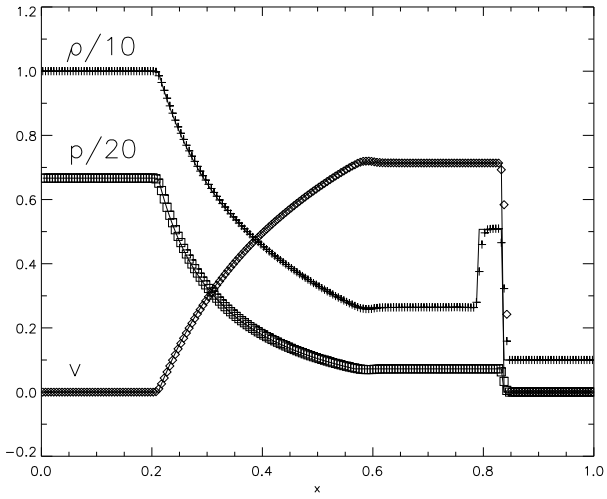

FIG. 10.—Exact (*solid lines*) and numerical profiles of pressure, density, and flow velocity along the diagonal normal to the initial discontinuity of the two-dimensional relativistic shock tube. The computations were performed on a uniform grid of 200 × 200 zones.

B3. A TWO-DIMENSIONAL TEST PROBLEM

The previous shock-tube test problem has also been used to check the behavior of our code in its two-dimensional Cartesian version. The initial numerical setup consists of a grid of 200 × 200 zones covering a unit square. The initial discontinuity is placed along one of the diagonals of the grid. Figure 10 shows a snapshot of the rest-mass density, the pressure, and the fluid flow velocity along the diagonal normal to the initial discontinuity. Again, the numerical solution is stable and represents the true flow pattern with very small errors except near discontinuities. The shock is resolved by ≈ 2–3 numerical zones.

REFERENCES

Akujor, C. E. 1992, A&A, 259, L61
Balsara, D. S., & Norman, M. L. 1992, ApJ, 393, 631
Begelman, M. C., Blandford, R. D., & Rees, M. J. 1984, Rev. Mod. Phys., 56, 255
Begelman, M. C., & Cioffi, D. C. 1989, ApJ, 345, L21
Begelman, M. C., Rees, M. J., & Blandford, R. G. 1979, Nature, 279, 770
Begelman, M. C., Rees, M. J., & Sikora, M. 1994, ApJ, 429, L57
Biretta, J. A., & Owen, F. N. 1990, in Parsec-scale Radio Jets, ed. J. A. Zensus & T. J. Pearson (Cambridge: Cambridge Univ. Press), 125
Biretta, J. A., Zhou, F., & Owen, F. N. 1995, ApJ, 447, 582
Blandford, R. D., & Königl, A. 1979, ApJ, 232, 34
Blandford, R. D., & Rees, M. J. 1974, MNRAS, 169, 395
Bodo, G., Massaglia, S., Ferrari, A., & Trussoni, E. 1994, A&A, 283, 655
Bowman, M. 1994, MNRAS, 269, 137
Bridle, A. H., & Perley, R. A. 1984, ARA&A, 22, 319
Clarke, D. A., Norman, M. L., & Burns, J. O. 1989, ApJ, 342, 700
Cohn, H. 1983, ApJ, 266, 73
Colella, P., & Woodward, P. R. 1984, J. Comput. Phys., 54, 174
Cox, C. I., Gull, S. F., & Scheuer, P. A. G. 1991, MNRAS, 252, 558
Daly, R. A., & Marscher, A. P. 1988, ApJ, 334, 539
Davis, R. J., Unwin, S. C., & Muxlow, T. W. B. 1991, Nature, 354, 374
Donat, R., & Marquina, A. 1996, J. Comput. Phys., 125, 42
Dubal, M. R., & Pantano, O. 1993, MNRAS, 261, 203
Duncan, G. C., & Hughes, P. A. 1994, ApJ, 436, L119
Eulderink, F., & Mellema, G. 1994, A&A, 284, 654
Fanaroff, B. L., & Riley, J. M. 1974, MNRAS, 167, 31
Ferrari, A., Trussoni, E., & Zaninetti, L. 1978, A&A, 64, 43
Font, J. A., Ibáñez, J. Mª., Marquina, A., & Martí, J. Mª. 1994, A&A, 282, 304
Ghisellini, G., Padovani, P., Celotti, A., & Maraschi, L. 1993, ApJ, 407, 65
Hardee, P. E., Clarke, D. A., & Howell, D. A. 1995, ApJ, 441, 644
Hooimeyer, J. R. A., Barthel, P. D., Schilizzi, R. T., & Miley, G. K. 1992, A&A, 261, 25
Hummel, C. A., et al. 1992, A&A, 257, 489
Königl, A. 1980, Phys. Fluids, 23, 1083
Kössl, D., & Müller, E. 1988, A&A, 206, 204
Kössl, D., Müller, E., & Hillebrandt, W. 1990, A&A, 229, 378
Krichbaum, T. P., Quirrenbach, A., & Witzel, A. 1992, in Variability of Blazars, ed. E. Valtaoja & M. J. Valtonen (Cambridge: Cambridge Univ. Press), 331
Laing, R. A. 1996, in ASP Conf. Proc. 100, Energy Transport in Radio Galaxies and Quasars, ed. P. E. Hardee, A. H. Bridle, & J. A. Zensus (San Francisco: ASP), 241
Lind, K. R., Payne, D. G., Meier, D. L., & Blandford, R. D. 1989, ApJ, 344, 89
Loken, C., Burns, J. O., Clarke, D. A., & Norman, M. L. 1992, ApJ, 392, 54
Loken, C., Roettiger, K., Burns, J. O., & Norman, M. L. 1995, ApJ, 445, 80
Martí, J. Mª., & Müller, E. 1994, J. Fluid Mech., 258, 317
———. 1996, J. Comput. Phys., 123, 1
Martí, J. Mª., Müller, E., Font, J. A., & Ibáñez, J. Mª. 1995, ApJ, 448, L105
Martí, J. Mª., Müller, E., & Ibáñez, J. Mª. 1994, A&A, 281, L9
Massaglia, S., Bodo, G., & Ferrari, A. 1996, A&A, 307, 997
Muxlow, T. W. B., & Garrington, S. T. 1991, in Beams and Jets in Astrophysics, ed. P. A. Hughes (Cambridge: Cambridge Univ. Press), 52
Norman, M. L., Burns, J. O., & Sulkanen, M. E. 1988, Nature, 335, 146
Norman, M. L., Smarr, L., & Winkler, K.-H. A. 1985, in Numerical Astrophysics, ed. J. Centrella (Boston: Jones & Bartlett)
Norman, M. L., Smarr, L., Winkler, K.-H. A., & Smith, M. D. 1982, A&A, 113, 285
Norman, M. L., Winkler, K.-H. A., & Smarr, L. 1983, in Astrophysical Jets, ed. A. Ferrari & A. G. Pacholczyk (Dordrecht: Reidel), 227
———. 1984, in Physics of Energy Transport in Extragalactic Radio Sources, ed. A. H. Bridle & J. A. Eilek (Green Bank, WV: NRAO), 150
Quirk, J. 1994, Int. J. Numer. Methods Fluids, 18, 555
Roe, P. 1981, J. Comput. Phys., 43, 357
Scheuer, P. A. G. 1974, MNRAS, 166, 513
———. 1982, in IAU Symp. 97, Extragalactic Radio Sources, ed. D. S. Heeschen & C. M. Wade (Dordrecht: Reidel), 163
Shu, C., & Osher, S. 1988, J. Comput. Phys., 77, 439
van Putten, M. H. P. M. 1993, ApJ, 408, L21
Wilson, M. J. 1987, MNRAS, 226, 447
Wilson, M. J., & Falle, S. A. E. G. 1985, MNRAS, 216, 971

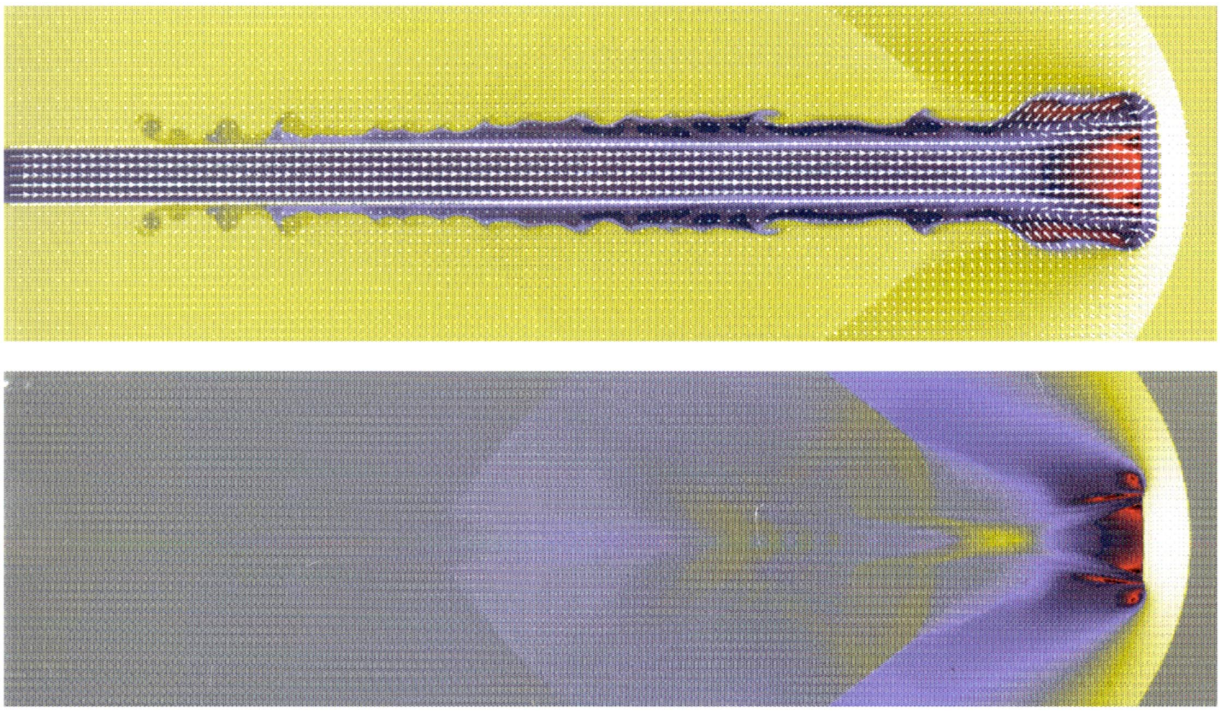

FIG. 1*a*

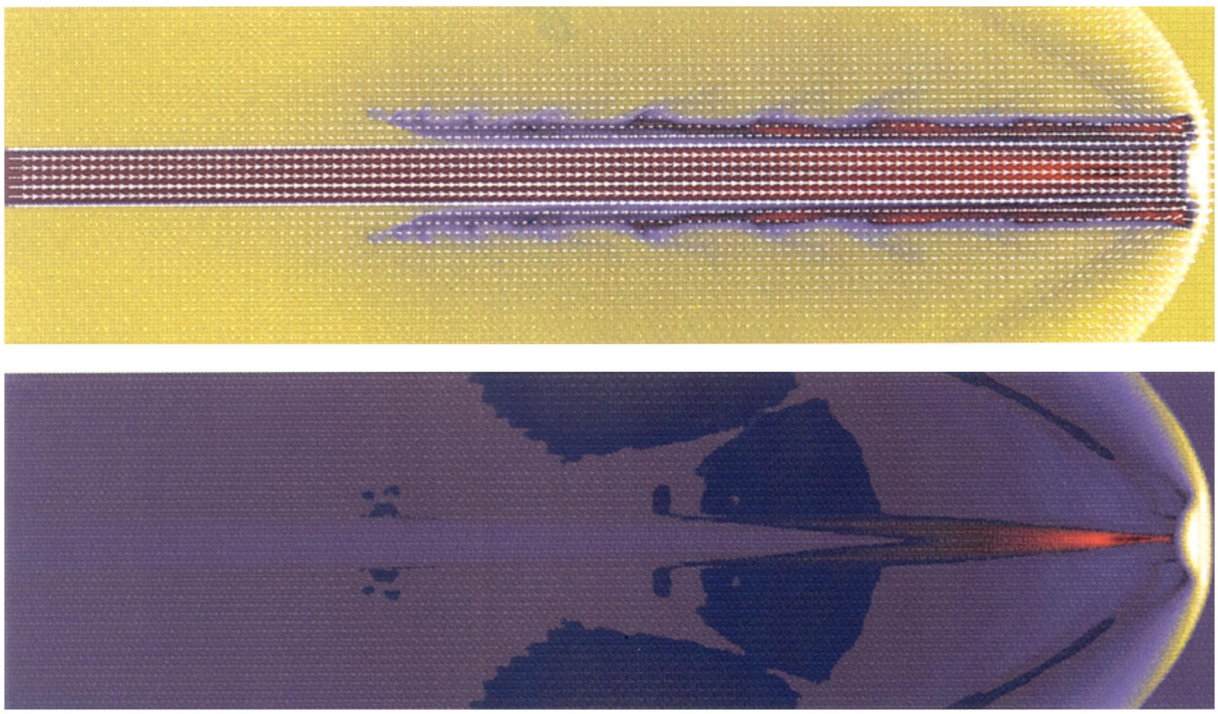

FIG. 1*b*

FIG. 1.—(*a*) Color-coded contour plots of the logarithm of the proper rest-mass density (*top*) and pressure (*bottom*) of model A1 ($\eta = 0.01$, $\gamma = 4/3$, $v_b = 0.99$, and $\mathcal{M}_b = 1.72$) at the end of the simulation, when the leading bow shock is about to leave the computational domain. The maximum values are coded in white ($\log \rho = 0.62$; $\log p = 0.50$). Decreasingly smaller values are coded in green, bright blue, dark blue, and red, and the minimum values are coded in black ($\log \rho = -3.04$; $\log p = -1.77$). The corresponding flow pattern is overlaid on the proper rest-mass density plot. Flow velocity vectors are plotted every fourth zone. The arrows within the beam and closer to the nozzle correspond to a flow velocity equal to v_b. (*b*) Same as (*a*), but for model A2 ($\eta = 0.01$, $\gamma = 4/3$, $v_b = 0.999$, and $\mathcal{M}_b = 1.74$). The maximum values are $\log \rho = 0.88$ and $\log p = 0.91$. The minimum values are $\log \rho = -2.50$ and $\log p = -1.32$. (*c*) Same as (*a*), but for model B1 ($\eta = 0.01$, $\gamma = 4/3$, $v_b = 0.99$, and $\mathcal{M}_b = 6.0$). The maximum values are $\log \rho = 0.91$ and $\log p = -0.25$. The minimum values are $\log \rho = -2.80$ and $\log p = -3.76$. (*d*) Same as (*a*), but for model B2 ($\eta = 0.01$, $\gamma = 4/3$, $v_b = 0.999$, and $\mathcal{M}_b = 6.0$). The maximum values are $\log \rho = 0.90$ and $\log p = 0.22$. The minimum values are $\log \rho = -2.79$ and $\log p = -3.64$. (*e*) Same as (*a*), but for model C1 ($\eta = 0.01$, $\gamma = 5/3$, $v_b = 0.9$, and $\mathcal{M}_b = 6.0$). The maximum values are $\log \rho = 0.66$ are $\log p = -1.51$. The minimum values are $\log \rho = -3.20$ and $\log p = -4.36$. (*f*) Same as (*a*), but for model C2 ($\eta = 0.01$, $\gamma = 5/3$, $v_b = 0.99$, and $\mathcal{M}_b = 6.0$). The maximum values are $\log \rho = 0.63$ and $\log p = -0.82$. The minimum values are $\log \rho = -2.93$ and $\log p = -4.17$. (*g*) Same as (*a*), but for model C3 ($\eta = 0.01$, $\gamma = 5/3$, $v_b = 0.999$, and $\mathcal{M}_b = 6.0$). The maximum values are $\log \rho = 0.73$ and $\log p = -0.41$. The minimum values are $\log \rho = -2.91$ and $\log p = -4.06$.

MARTÍ et al. (see 479, 156)

PLATE 1

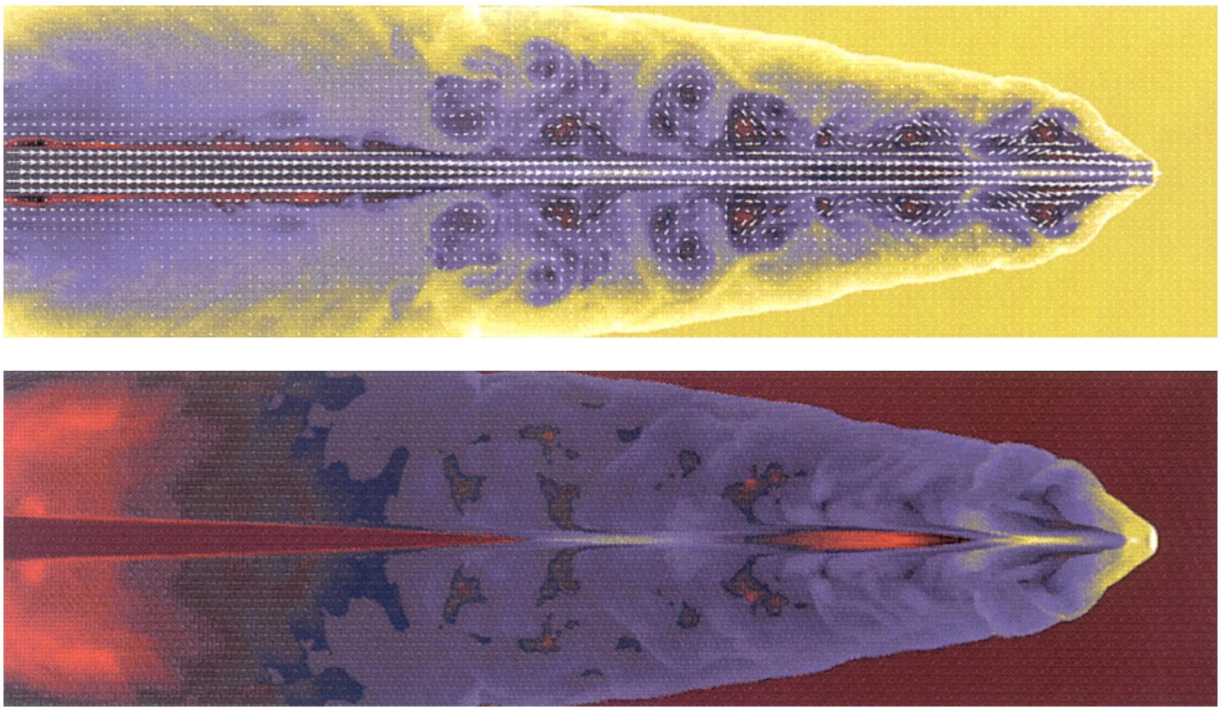

FIG. 1*c*

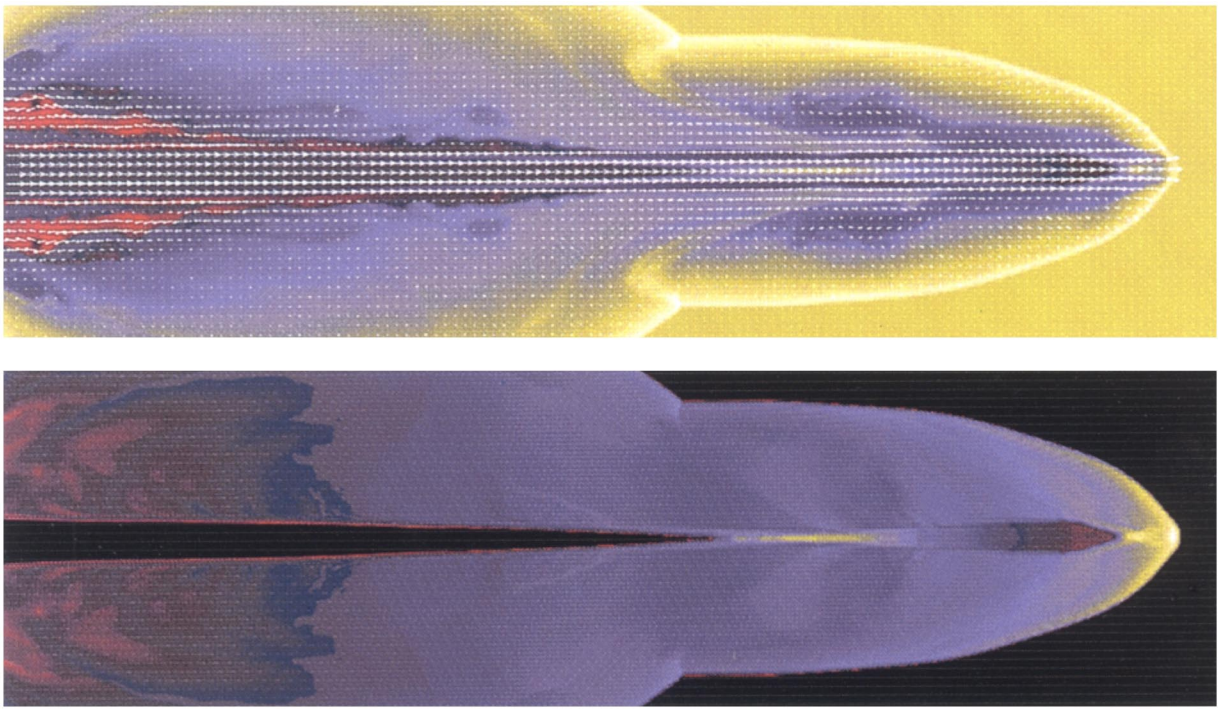

FIG. 1*d*

MARTÍ et al. (see 479, 156)

PLATE 2

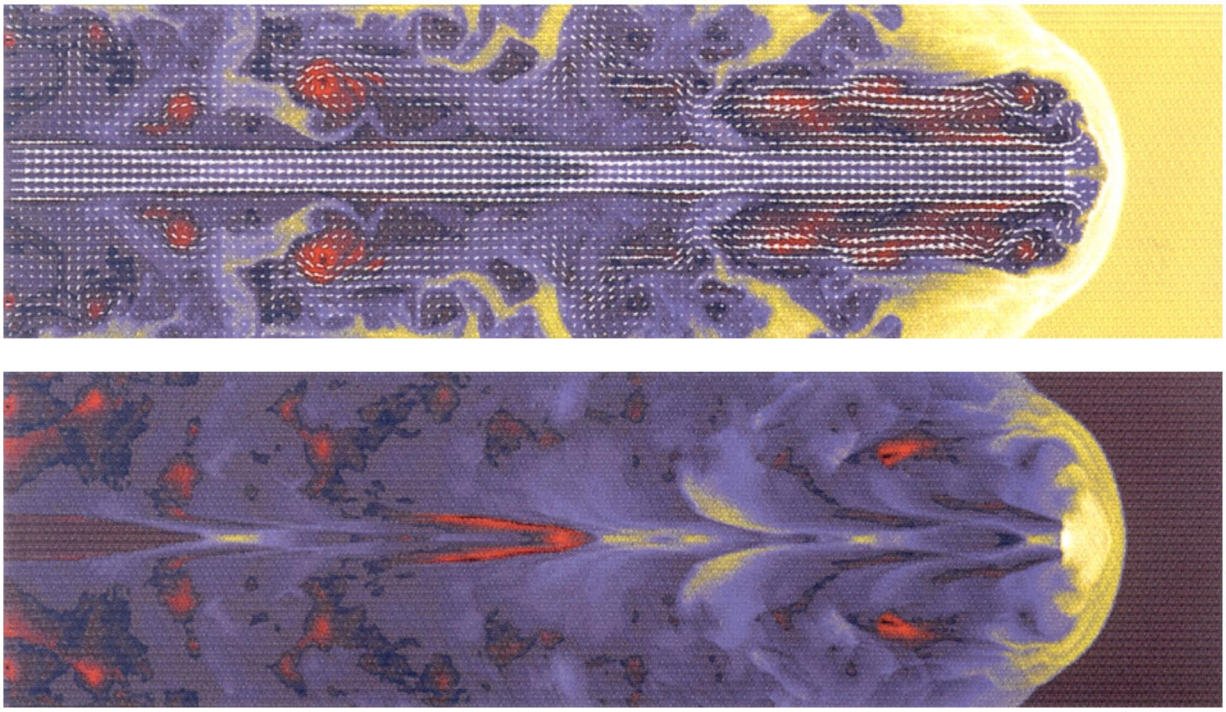

FIG. 1*e*

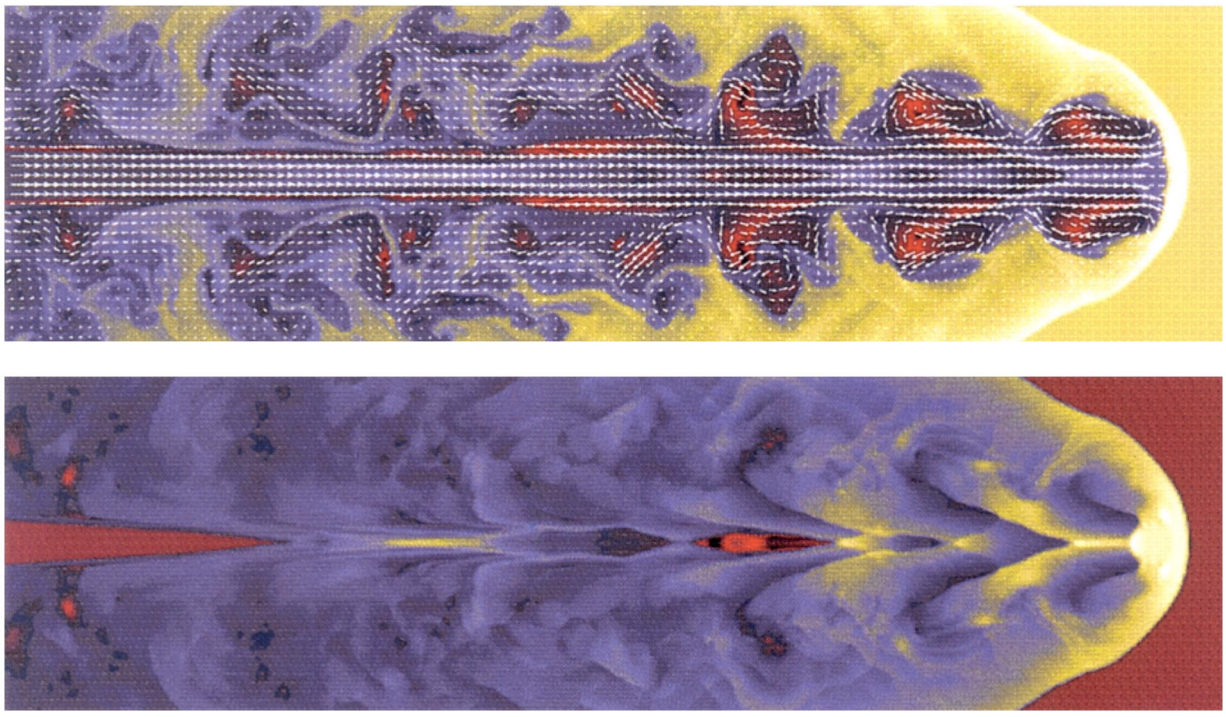

FIG. 1*f*

MARTÍ et al. (see 479, 156)

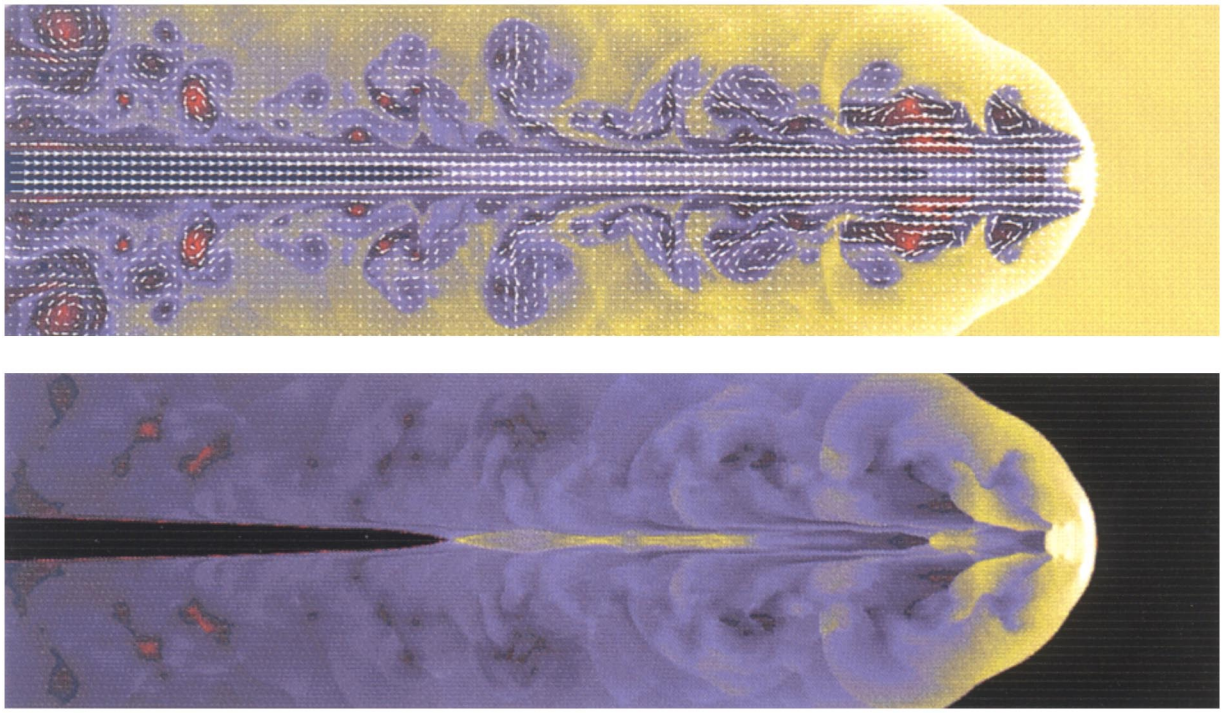

FIG. 1*g*

MARTÍ et al. (see 479, 156)

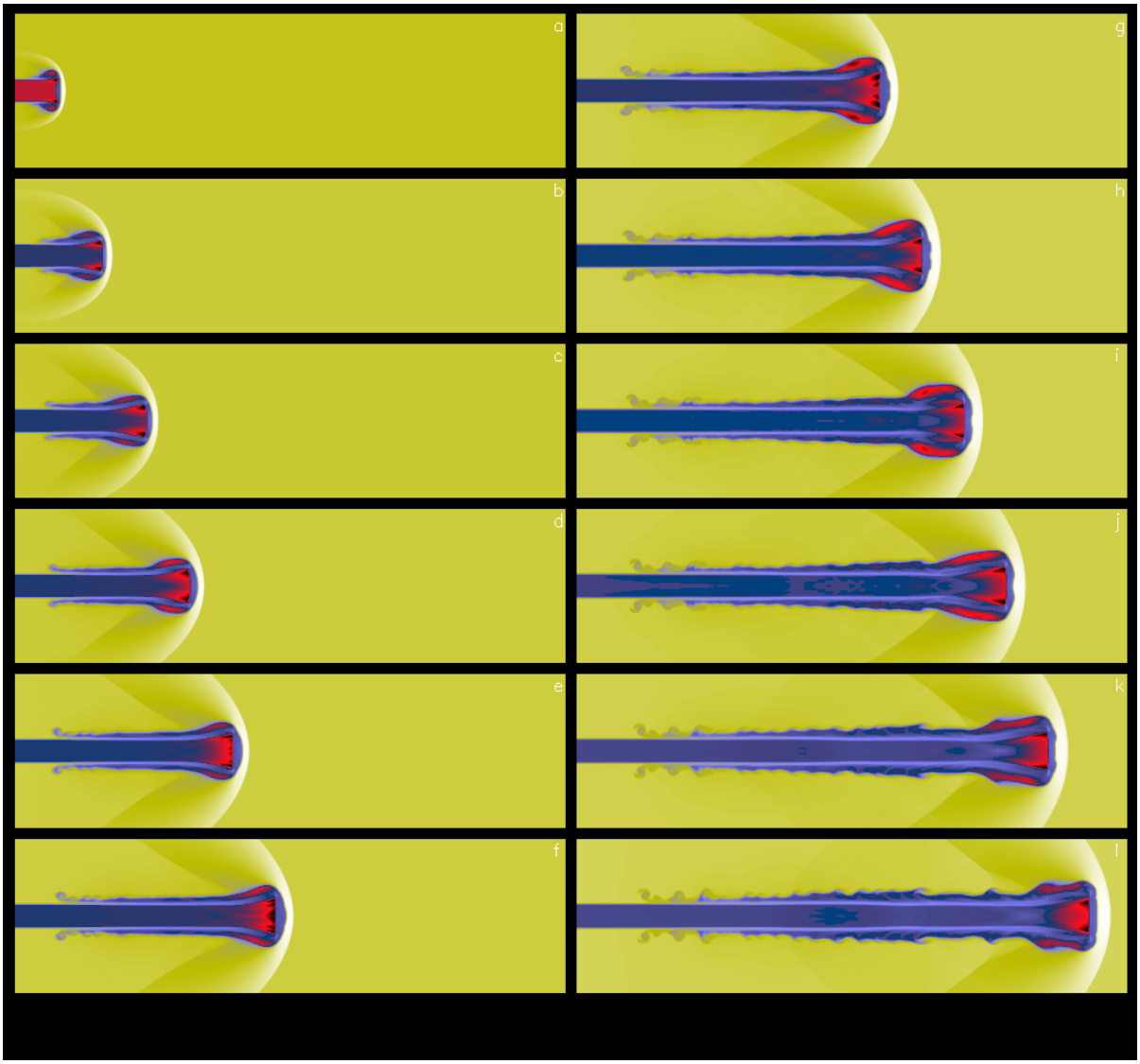

FIG. 2*a*

FIG. 2.—(*a*) Twelve snapshots of the time evolution of the relativistic jet model A1 ($\eta = 0.01$, $\gamma = 4/3$, $v_b = 0.99c$, and $\mathcal{M}_b = 1.72$). The logarithm of the proper rest-mass density is shown at times $t = 5.01$ (a), 10.01 (b), 15.01 (c), 20.01 (d), 25.01 (e), 30.01 (f), 35.01 (g), 40.02 (h), 45.02 (i), 50.02 (j), 55.03 (k), and 60.04 (l). Time is in units of R_b/c. The color coding is the same as in Fig. 1*a*. Note the extremely thin cocoon, with the majority of its material located in the lobe at the head. Note also the naked beam near the source (for further discussion, see text). (*b*) Same as (*a*), but showing the logarithm of the pressure. Note the absence of any internal structure inside the beam, as it and the cocoon/shocked external medium are in pressure equilibrium. Also note the constant thickness of the terminal Mach disk (for further discussion, see text).

MARTÍ et al. (see 479, 156)

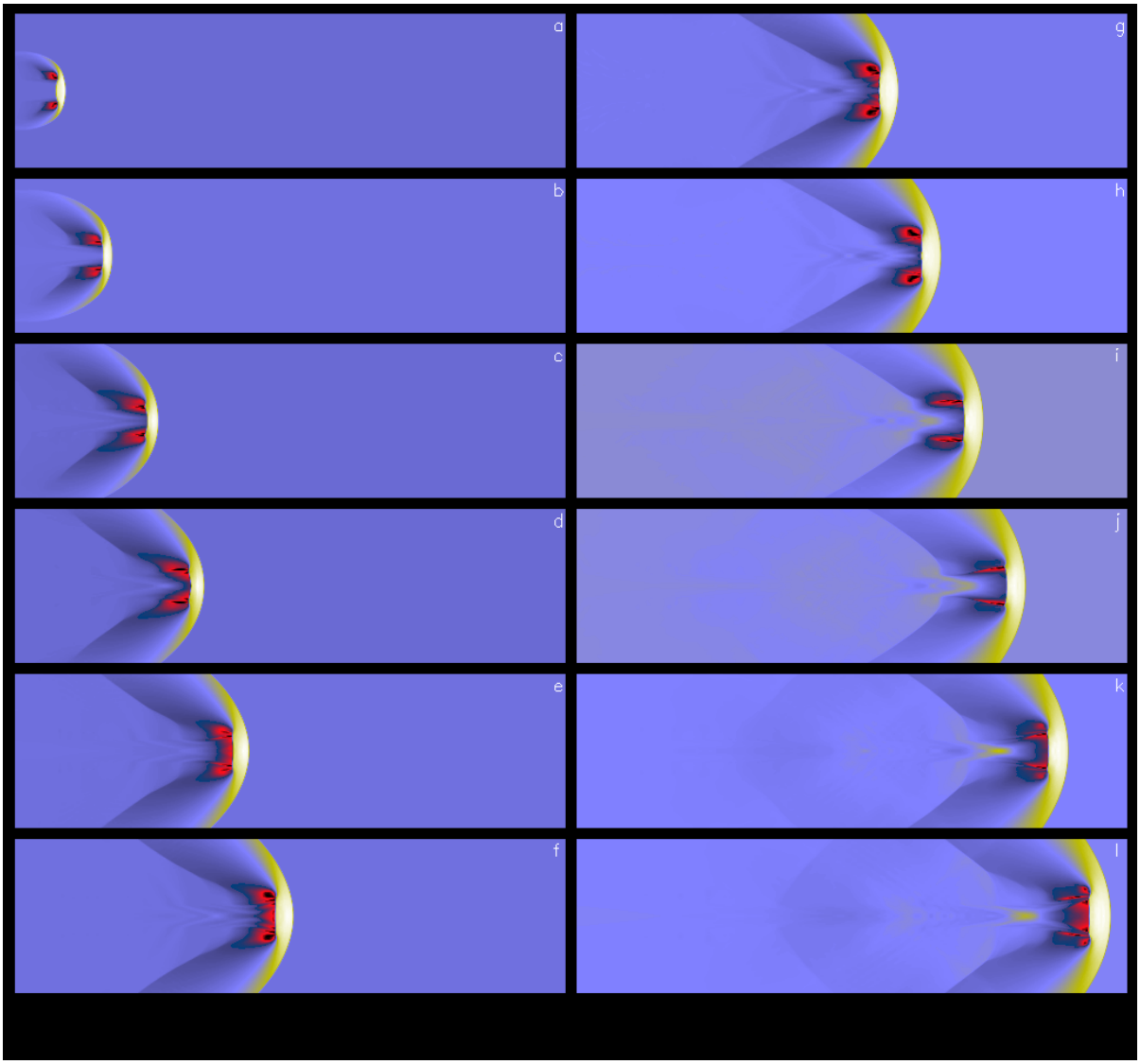

FIG. 2*b*

MARTÍ et al. (see 479, 157)

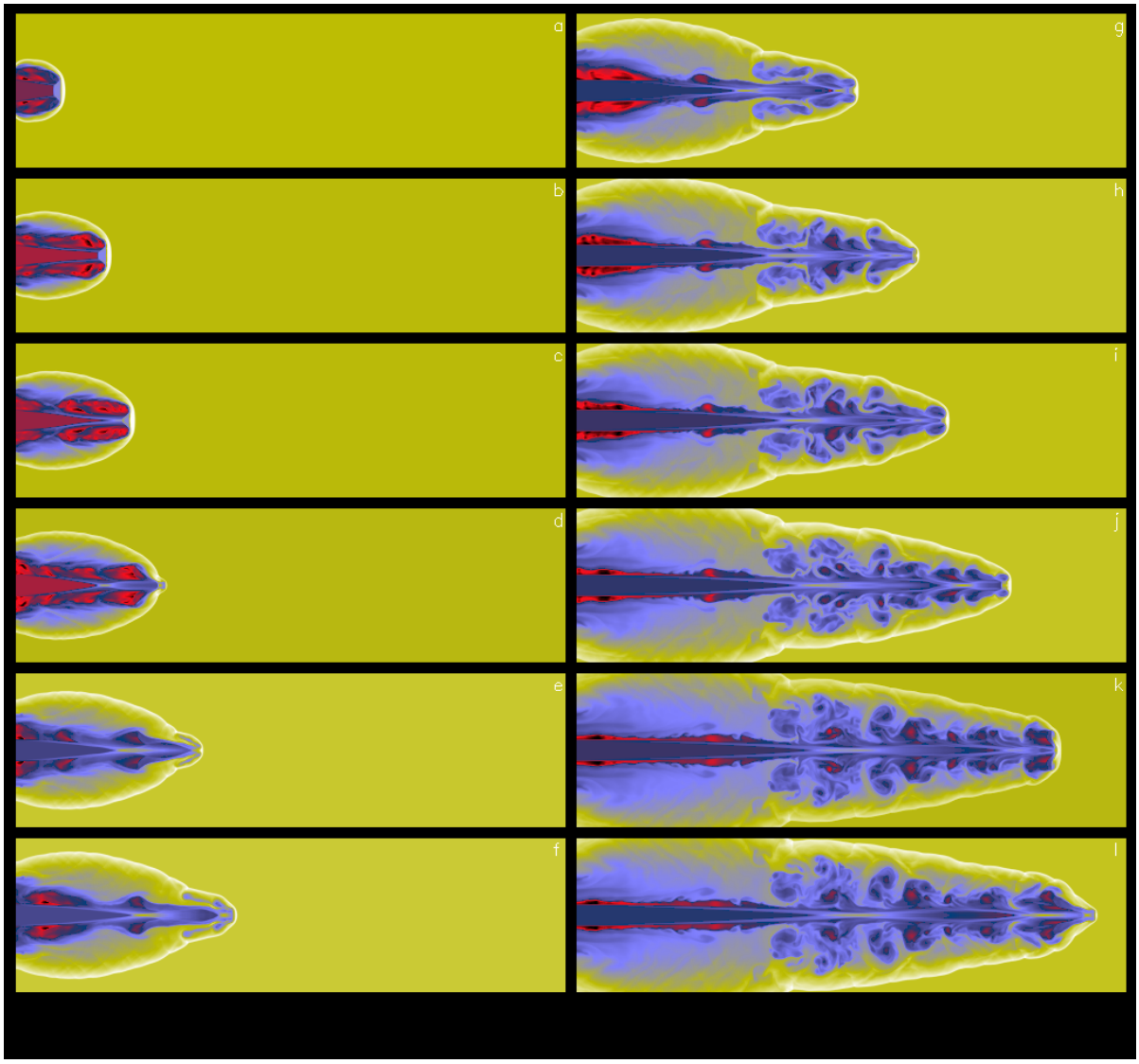

FIG. 3*a*

FIG. 3.—(*a*) Same as Fig. 2*a*, but showing the time evolution of the relativistic jet model B1 ($\eta = 0.01$, $\gamma = 4/3$, $v_b = 0.99$, and $\mathcal{M}_b = 6.0$). The logarithm of the proper rest-mass density is shown at times $t = 10.01$ (a), 20.02 (b), 25.03 (c), 30.03 (d), 35.04 (e), 40.04 (f), 50.05 (g), 60.06 (h), 65.07 (i), 75.08 (j), 85.09 (k), and 90.10 (l). Time is in units of R_b/c. The color coding is the same as in Fig. 1*a*. Note the acceleration of the head of the jet in frames (d) and (l) and the unstable and turbulent structure of the thin cocoon (for further discussion, see text). (*b*) Same as (*a*), but showing the logarithm of the pressure. Note the overpressured cocoon and the presence of a terminal Mach disk of diminishing cross section in the first two frames and the subsequent appearance of internal shock waves inside the beam (for further discussion, see text).

MARTÍ et al. (see 479, 156)

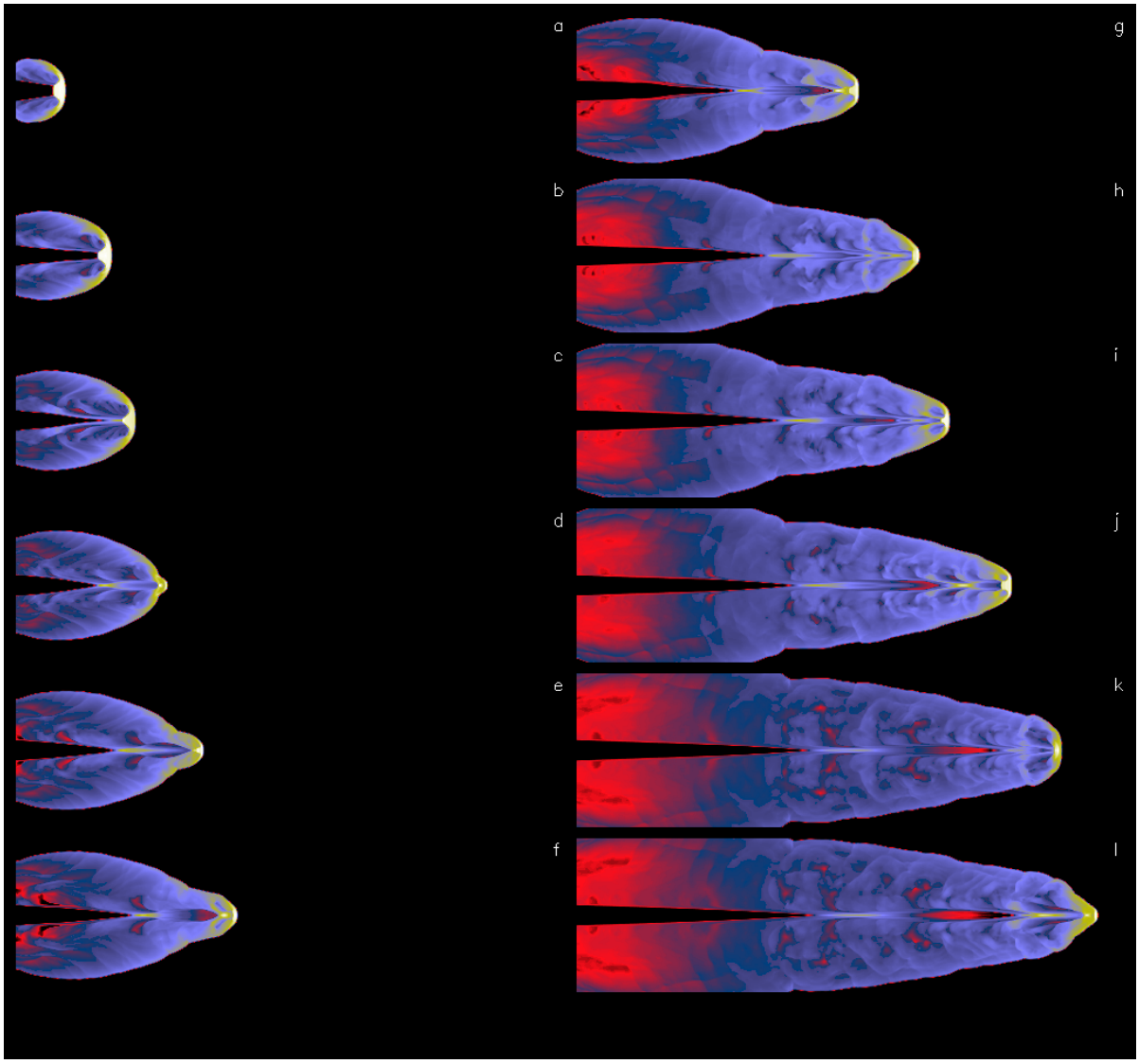

FIG. 3*b*

MARTÍ et al. (see 479, 157)

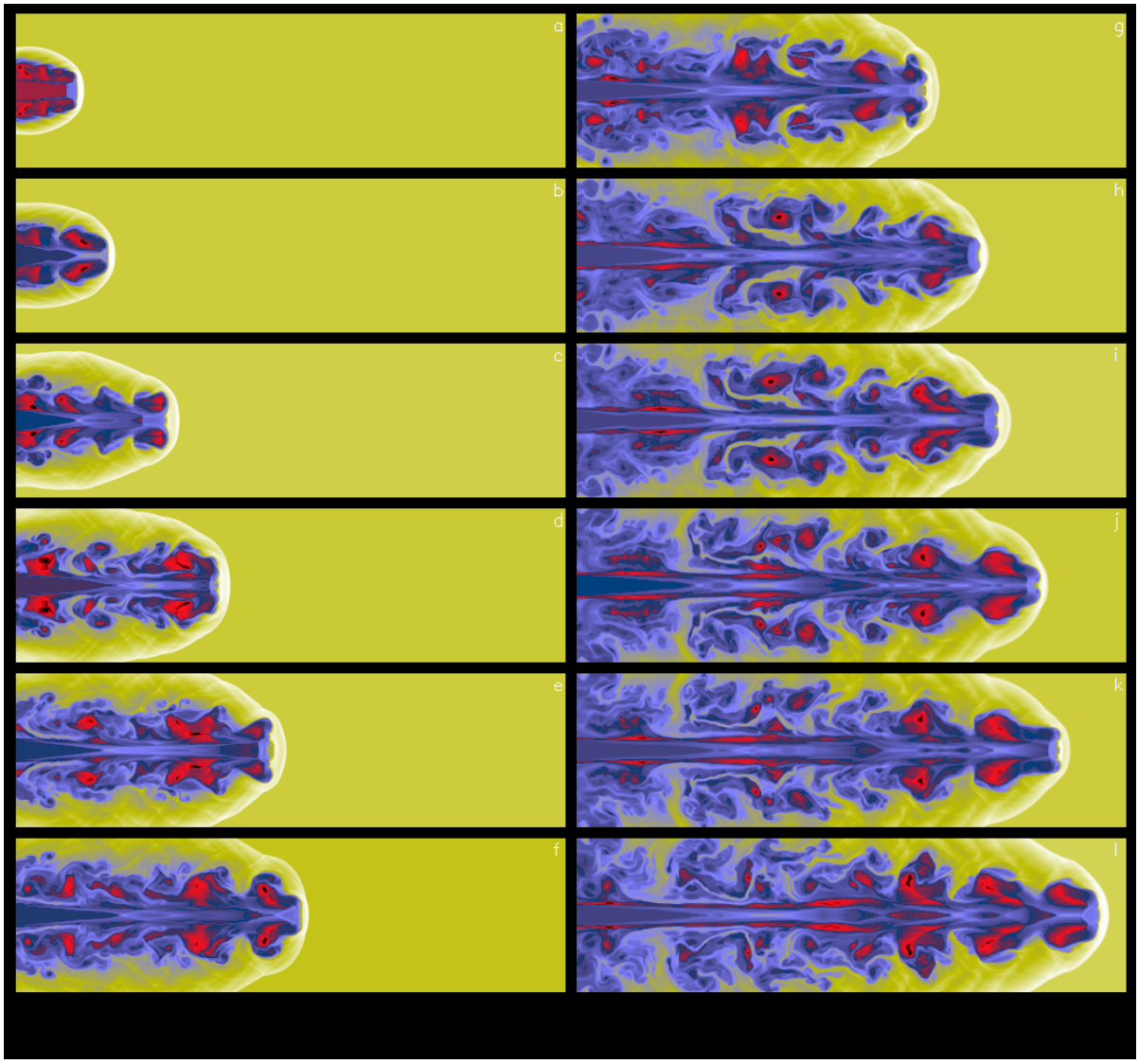

FIG. 4*a*

FIG. 4.—(*a*) Same as Fig. 2*a*, but showing the time evolution of the relativistic jet model C2 ($\eta = 0.01$, $\gamma = 5/3$, $v_b = 0.99$, and $\mathcal{M}_b = 6.0$). The logarithm of the proper rest-mass density is shown at times $t = 14.01$ (a), 21.01 (b), 35.02 (c), 49.02 (d), 63.03 (e), 70.03 (f), 87.54 (g), 100.17 (h), 105.18 (i), 115.20 (j), 120.21 (k), and 130.23 (l). Time is in units of R_b/c. The color coding is the same as in Fig. 1*a*. Comparing with Fig. 3*a*, note the presence of a more extended cocoon, also Kelvin-Helmholtz unstable, and the absence of any significant acceleration of the jet head. The vortex-shedding mechanism is clearly visible in some of the frames (for further discussion, see text). (*b*) Same as (*a*), but showing the logarithm of the pressure. As in model B1 (Fig. 3), note the rich internal structure within the beam and the presence of an overpressured cocoon (for further discussion, see text).

MARTÍ et al. (see 479, 156)

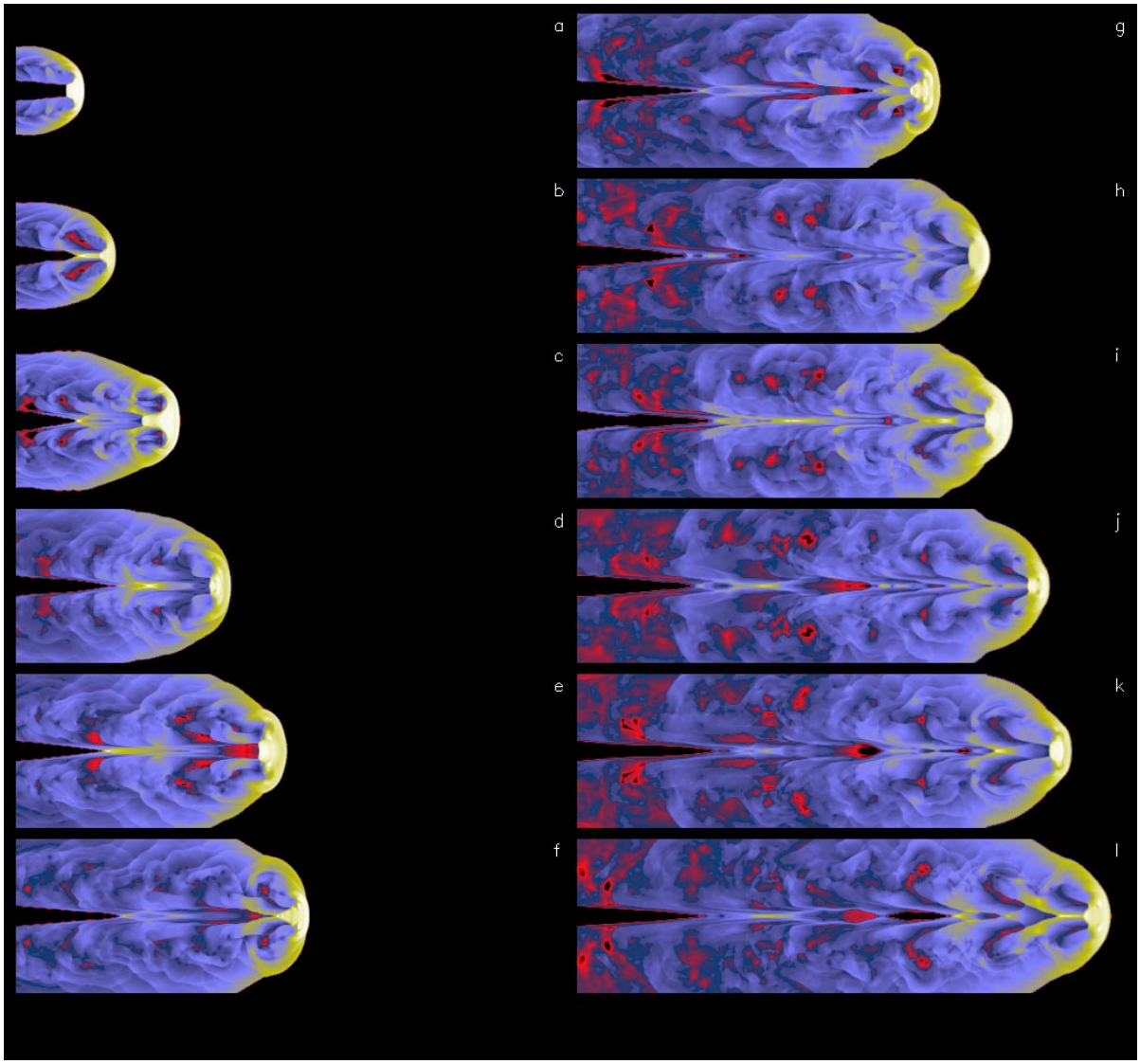

FIG. 4*b*

MARTÍ et al. (see 479, 157)